

Diffusion Tensor Analysis With Invariant Gradients and Rotation Tangents

Gordon Kindlmann*, Daniel B. Ennis, Ross T. Whitaker, *Member, IEEE*, and Carl-Fredrik Westin

Abstract—Guided by empirically established connections between clinically important tissue properties and diffusion tensor parameters, we introduce a framework for decomposing variations in diffusion tensors into changes in *shape* and *orientation*. Tensor shape and orientation both have three degrees-of-freedom, spanned by invariant gradients and rotation tangents, respectively. As an initial demonstration of the framework, we create a tunable measure of tensor difference that can selectively respond to shape and orientation. Second, to analyze the spatial gradient in a tensor volume (a third-order tensor), our framework generates edge strength measures that can discriminate between different neuroanatomical boundaries, as well as creating a novel detector of white matter tracts that are adjacent yet distinctly oriented. Finally, we apply the framework to decompose the fourth-order diffusion covariance tensor into individual and aggregate measures of shape and orientation covariance, including a direct approximation for the variance of tensor invariants such as fractional anisotropy.

Index Terms—Diffusion tensor magnetic resonance imaging (MRI), fourth-order covariance tensor, tensor feature detection, tensor invariants, third-order gradient tensor.

I. INTRODUCTION

DIFFUSION tensor imaging (DTI) enables noninvasive measurements of microstructural orientation and organization in biological tissue, such as the central nervous system or cardiac muscle [1], [2], and has found numerous applications in neuroscience, medicine, and bioengineering [3]–[10]. Research in tensor-valued image processing takes on greater significance in DTI, given the empirically established connections between mathematical properties of diffusion tensors, and biological properties of tissue. For example, the average of the tensor eigenvalues indicates bulk mean diffusivity, used in ischemic stroke detection [11], [12]. Dissimilarity among the eigenvalues (anisotropy) indicates the strength of microstructural organization [13], [14]. The principal eigenvector (the direction of greatest diffusivity) indicates the approximate direction of

axonal pathways and muscle myofibers [15]–[18]. Ideally, the same biological connections can inform and enhance research in diffusion tensor image processing, which uses mathematical methods of increasing sophistication and abstraction.

A common theme in DTI processing is quantifying *difference* and *variation* of tensors. This includes difference measures (or equivalently, similarity measures) between two tensors, as well as structure tensors. Difference measures play a role in a variety of DTI algorithms, for example image registration [19], [20], edge-preserving filtering [21]–[23], and segmentation [24]–[26]. Local differential structure can also be measured with a second-order *structure tensor*, a sum of tensor products of gradients [27]–[29]. Structure tensors of diffusion tensor components have been used for visually detecting tissue interfaces [30], anisotropic interpolation [31], and edge-preserving filtering [32].

Local variation in diffusion tensor fields can also be measured by higher-order tensors. The gradient of a smooth second-order diffusion tensor field is a third-order tensor [33], introduced in DTI by Pajevic *et al.* as part of their spline-based tensor interpolation [34]. Such gradients can also figure in tensor-based registration, to analytically compute the derivative of the optimization function [20], [35], and in DTI segmentation, as an edge strength measure [36]. Alternatively, the covariance of a set of second-order tensors is a fourth-order tensor, recently used by Basser and Pajevic to describe tensor distributions from noisy diffusion-weighted images (DWIs) [37], [38], and by Lenglet *et al.* for modeling distributions of tensors on a Riemannian manifold [39].

In our view, some of the previous work above quantifies tensor differences, gradients, or covariance in an overly broad manner, by not distinguishing between the different tensor parameters that make DTI a uniquely powerful modality. Based upon empirically established connections between diffusion tensor parameters and underlying tissue attributes, we present in Section II a novel framework by which diffusion tensor analysis can be expressed and refined in terms of biologically meaningful quantities. The framework generates an orthonormal coordinate system around each tensor value, decomposing the tensor's six degrees-of-freedom into *shape* and *orientation*. Tensor shape includes mean diffusivity and anisotropy, and orientation includes the principal diffusion direction. The three *invariant gradients* (gradients of invariants) in our framework describe variations in tensor shape, and the three *rotation tangents* capture variations in tensor orientation.

Our framework enables novel decompositions of third-order diffusion gradient tensors and fourth-order diffusion covariance tensors, as described in Section III. Specific contributions, demonstrated in Section IV, include the ability to isolate

Manuscript received June 12 2007; revised August 16, 2007. This work was supported by the National Institutes of Health (NIH) under Grants NIBIB T32-EB002177 (GK), Grant K99-HL087614 (DBE), Grant U41-RR019703 (CFW), Grant R01-MH074794 (CFW, GK), Grant NCRR P41-RR13218 (CFW), and Grant U54-EB005149 (RTW). *Asterisk indicates corresponding author.*

*G. Kindlmann is with the Department of Radiology, Brigham and Womens Hospital, Harvard Medical School, Cambridge, MA 02139 USA (e-mail: gk@bwh.harvard.edu).

D. B. Ennis is with the Department of Cardiothoracic Surgery, Stanford University, Stanford, CA 94305 USA.

R. T. Whitaker is with the School of Computing, University of Utah, Salt Lake City, UT 84112 USA.

C.-F. Westin is with the Department of Radiology, Brigham and Womens Hospital, Harvard Medical School, Cambridge, MA 02139 USA.

Digital Object Identifier 10.1109/TMI.2007.907277

TABLE I
MATHEMATICAL CONVENTIONS AND NOTATION

$\mathbb{R}^3 \otimes \mathbb{R}^3$	space of second-order tensors	$\tilde{\mathbf{A}}$	$= \mathbf{A} - \overline{\mathbf{A}}$, deviatoric of \mathbf{A}
Sym_3	symmetric tensors in $\mathbb{R}^3 \otimes \mathbb{R}^3$	$\{\lambda_i\}, \{\mathbf{e}_i\}$	eigenvalues, eigenvectors of \mathbf{D} $\mathbf{D} = \lambda_i \mathbf{e}_i \otimes \mathbf{e}_i$; $\lambda_1 \geq \lambda_2 \geq \lambda_3$
SO_3	rotations on \mathbb{R}^3	$\{K_i\}, \{R_i\}$	sets of orthogonal invariants $K_1 = \text{trace}$; $R_2 = \text{FA}$; $K_3 = R_3 = \text{mode}$
$\mathcal{B} = \{\mathbf{b}_i\}_{i=1,2,3}$	orthonormal basis for \mathbb{R}^3	$\{\widehat{\nabla}_D K_i(\mathbf{D})\}$	cylindrical invariant gradients
δ_{ij}	$\delta_{ij} = 1$ if $i = j$, 0 otherwise	$\{\widehat{\nabla}_D R_i(\mathbf{D})\}$	spherical invariant gradients
\mathbf{v}	vector in \mathbb{R}^3	$\{\widehat{\Phi}_i(\mathbf{D})\}$	rotation tangents, basis for orientation variation around \mathbf{D}
$v = [\mathbf{v}]_{\mathcal{B}}$	$v_i = \mathbf{v} \cdot \mathbf{b}_i$ matrix representation of \mathbf{v} in \mathcal{B}	\mathcal{G} ; $G = [\mathcal{G}]$	third-order tensor in $\text{Sym}_3 \otimes \mathbb{R}^3$
\mathbf{D}	second-order tensor in Sym_3	$\mathbf{F}(\mathbf{x})$	tensor field; the DTI volume
$D = [\mathbf{D}]_{\mathcal{B}}$	$D_{ij} = \mathbf{b}_i \cdot \mathbf{D} \mathbf{b}_j$ matrix representation of \mathbf{D} in \mathcal{B}	$\mathbf{D} : \mathcal{G}$	$= D_{ij} G_{ijk} \mathbf{b}_k \in \mathbb{R}^3$ contraction of \mathcal{G} with \mathbf{D}
\mathbf{I}	identity tensor in $\mathbb{R}^3 \otimes \mathbb{R}^3$	∇J	$= \nabla_D J : \nabla \mathbf{F}$, spatial gradient of J in \mathbf{F}
$\mathbf{u} \otimes \mathbf{v}$	$\in \mathbb{R}^3 \otimes \mathbb{R}^3$, $[\mathbf{u} \otimes \mathbf{v}]_{ij} = u_i v_j$ tensor product of \mathbf{u} and \mathbf{v}	$\widehat{\nabla} J$	$= \widehat{\nabla}_D J : \nabla \mathbf{F}$, projected gradient of J
$\mathbf{A} : \mathbf{B}$	$= \text{tr}(\mathbf{A} \mathbf{B}^T) = A_{ij} B_{ij} \in \mathbb{R}$ contraction of \mathbf{A} and \mathbf{B}	$\widehat{\nabla} \phi_i$	$= \widehat{\Phi}_i : \nabla \mathbf{F}$, spatial “gradient” of \mathbf{e}_i rotation
$ \mathbf{A} $	$= \sqrt{\mathbf{A} : \mathbf{A}}$, tensor norm of \mathbf{A}	\mathbf{S} ; $S = [\mathbf{S}]$	fourth-order tensor in $\text{Sym}_3 \otimes \text{Sym}_3$
$\overline{\mathbf{A}}$	$= \text{tr}(\mathbf{A}) \mathbf{I} / 3$, isotropic part of \mathbf{A}	$\mathbf{A} : \mathbf{S} : \mathbf{B}$	$= A_{ij} S_{ijkl} B_{kl} \in \mathbb{R}$ contraction of \mathbf{S} with \mathbf{A} and \mathbf{B}

boundaries in tensor shape and orientation, a detector (“adjacent orthogonality”) of adjacent but orthogonal fiber tracts, the intuitive visualization of fourth-order diffusion covariance tensor fields as a 6×6 image matrix, and aggregate measures of the variance and covariance of tensor shape and orientation. This paper is a simplified exposition and expanded application of the framework initially described in [40], leveraging our previous work on orthogonal invariant sets [41].

II. THEORETICAL AND BIOLOGICAL BACKGROUND

Our notational conventions are as follows (see Table I for reference). $\mathbb{R}^3 \otimes \mathbb{R}^3$ is the set of second-order tensors in three-dimensional space \mathbb{R}^3 [42]. In a basis $\mathcal{B} = \{\mathbf{b}_1, \mathbf{b}_2, \mathbf{b}_3\}$ for \mathbb{R}^3 , a typical vector \mathbf{v} or tensor \mathbf{D} has matrix representation $v = [\mathbf{v}]_{\mathcal{B}}$ or $D = [\mathbf{D}]_{\mathcal{B}}$, respectively, or simply $[\mathbf{v}]$ or $[\mathbf{D}]$ when the basis is assumed. Our work considers only orthonormal bases ($\mathbf{b}_i \cdot \mathbf{b}_j = \delta_{ij}$): all of our tensors are Cartesian, with no distinction between covariant and contravariant indices. The contraction of two tensors, analogous to a vector dot product, is $\mathbf{A} : \mathbf{B} = \text{tr}(\mathbf{A} \mathbf{B}^T)$. Tensor norm $|\mathbf{A}| = \sqrt{\mathbf{A} : \mathbf{A}}$ is the Frobenius norm of matrix $[\mathbf{A}]$. Tensor \mathbf{A} is decomposed into isotropic and deviatoric parts, $\overline{\mathbf{A}} = \text{tr}(\mathbf{A}) \mathbf{I} / 3$ and $\tilde{\mathbf{A}} = \mathbf{A} - \overline{\mathbf{A}}$, respectively. We use Einstein notation: a repeated index within a term implies summation over that index, e.g., $D_{ij} v_j = \sum_{j=1}^3 D_{ij} v_j$; and $D_{ij} \mathbf{b}_i \otimes \mathbf{b}_j = \sum_{i=1}^3 \sum_{j=1}^3 D_{ij} \mathbf{b}_i \otimes \mathbf{b}_j$.

Our framework is based upon the recognition that tensors are linear transforms, and that linear transforms constitute a vector space. Linear transforms from \mathbb{R}^3 to \mathbb{R}^3 form a vector space isomorphic to \mathbb{R}^9 [43]. The tensor product $\mathbf{u} \otimes \mathbf{v}$ is a linear transform defined by $(\mathbf{u} \otimes \mathbf{v}) \mathbf{w} = \mathbf{u}(\mathbf{v} \cdot \mathbf{w})$ for all \mathbf{w} in \mathbb{R}^3 [33]. Any linear transform \mathbf{T} can be expressed as a linear combination of tensor products of orthonormal basis vectors \mathbf{b}_i , according to $\mathbf{T} = T_{ij} \mathbf{b}_i \otimes \mathbf{b}_j$ and $T_{ij} = \mathbf{b}_i \cdot \mathbf{T} \mathbf{b}_j$. Tensor contraction $\mathbf{A} : \mathbf{B}$ is an inner product on $\mathbb{R}^3 \otimes \mathbb{R}^3$, and we say \mathbf{A} and \mathbf{B} are orthogonal when $\mathbf{A} : \mathbf{B} = 0$.

Sym_3 denotes the set of *symmetric* tensors ($\mathbf{D}^T = \mathbf{D}$) in $\mathbb{R}^3 \otimes \mathbb{R}^3$. A diffusion tensor \mathbf{D} is a symmetric linear transform that maps (by Fick’s first law) from concentration gradient vector ∇c to diffusive flux vector $\mathbf{j} = -\mathbf{D} \nabla c$ [1], [44]. Symmetric tensors have real eigenvalues and three orthogonal real eigenvectors. A *principal frame* $\mathcal{E} = \{\mathbf{e}_i\}$ is an orthonormal \mathbb{R}^3 basis of eigenvectors of tensor \mathbf{D} , which diagonalizes the matrix $[\mathbf{D}]_{\mathcal{E}} = \text{diag}(\lambda_1, \lambda_2, \lambda_3)$. The *spectral decomposition* $\mathbf{D} = \lambda_i \mathbf{e}_i \otimes \mathbf{e}_i$ is a coordinate-free expression of a tensor \mathbf{D} in terms of its eigensystem. Diffusion tensors are also positive-definite [1], the significance of which for diffusion tensor image processing is discussed in Section V-B.

Sym_3 is a six-dimensional vector space. To demonstrate, we form an orthonormal basis $\mathcal{B} = \{\mathbf{B}_i\}_{i=1..6}$ for Sym_3 from an orthonormal basis $\mathcal{B} = \{\mathbf{b}_i\}_{i=1,2,3}$ for \mathbb{R}^3 .

$$\left. \begin{aligned} \mathbf{B}_1 &\equiv \mathbf{b}_1 \otimes \mathbf{b}_1 \\ \mathbf{B}_2 &\equiv (\mathbf{b}_1 \otimes \mathbf{b}_2 + \mathbf{b}_2 \otimes \mathbf{b}_1) / \sqrt{2} \\ \mathbf{B}_3 &\equiv (\mathbf{b}_1 \otimes \mathbf{b}_3 + \mathbf{b}_3 \otimes \mathbf{b}_1) / \sqrt{2} \\ \mathbf{B}_4 &\equiv \mathbf{b}_2 \otimes \mathbf{b}_2 \\ \mathbf{B}_5 &\equiv (\mathbf{b}_2 \otimes \mathbf{b}_3 + \mathbf{b}_3 \otimes \mathbf{b}_2) / \sqrt{2} \\ \mathbf{B}_6 &\equiv \mathbf{b}_3 \otimes \mathbf{b}_3 \end{aligned} \right\}. \quad (1)$$

Tensors in Sym_3 can be decomposed into vector components by $\mathbf{D} = D_i \mathbf{B}_i$ and $D_i = \mathbf{D} : \mathbf{B}_i$. We use bold subscripts i to index components of Sym_3 considered as vectors rather than tensors. We define \mathcal{B} to serve as a point of comparison for our framework, and to convert between the D_{ij} components of matrix $[\mathbf{D}]_{\mathcal{B}}$ and the D_i components of six-vector $[\mathbf{D}]_{\mathcal{B}}$

$$[\mathbf{D}]_{\mathcal{B}} = \begin{bmatrix} D_{11} \\ \sqrt{2} D_{12} \\ \sqrt{2} D_{13} \\ D_{22} \\ \sqrt{2} D_{23} \\ D_{33} \end{bmatrix}, [\mathbf{D}]_{\mathcal{B}} = \begin{bmatrix} D_1 & D_2 / \sqrt{2} & D_3 / \sqrt{2} \\ \text{sym} & D_4 & D_5 / \sqrt{2} \\ & & D_6 \end{bmatrix}. \quad (2)$$

The tensor norm of D_{ij} equals the vector length of D_i

$$|\mathbf{D}| = \sqrt{\mathbf{D} : \mathbf{D}} = \sqrt{D_{ij}D_{ij}} = \sqrt{D_i D_i}. \quad (3)$$

Our basic strategy in this work is to create *at each tensor* \mathbf{D} a local orthonormal Sym_3 basis, with basis vectors (or “basis tensors”) aligned with biologically meaningful degrees-of-freedom. These include *shape* and *orientation*, which we distinguish by considering tensor rotation. Given a rotation \mathbf{R} in SO_3 , the group of rotations on \mathbb{R}^3 , the group action ψ defines a mapping on Sym_3 by

$$\begin{aligned} \psi : \text{SO}_3 \times \text{Sym}_3 &\mapsto \text{Sym}_3 \\ \psi(\mathbf{R}, \mathbf{D}) &\equiv \mathbf{RDR}^\top. \end{aligned} \quad (4)$$

The orbit $\text{SO}_3(\mathbf{D})$ of a tensor \mathbf{D} is the set of all possible values of $\psi(\mathbf{R}, \mathbf{D})$, which is all possible reorientations of \mathbf{D}

$$\text{SO}_3(\mathbf{D}) \equiv \{\mathbf{RDR}^\top | \mathbf{R} \in \text{SO}_3\}. \quad (5)$$

The group properties of SO_3 ensure that orbits of ψ partition Sym_3 into equivalence classes [45]: every tensor is on some orbit, and two orbits are either disjoint or equal. Orbits of ψ contain all tensor orientations, so we say that tensors \mathbf{D}_0 and \mathbf{D}_1 have the same *shape* if they are on the same orbit of ψ .

An invariant $J : \text{Sym}_3 \mapsto \mathbb{R}$ is a scalar-valued function of tensors that is constant on orbits of $\psi : \text{SO}_3(\mathbf{D}_0) = \text{SO}_3(\mathbf{D}_1) \Rightarrow J(\mathbf{D}_0) = J(\mathbf{D}_1)$. Trace $\text{tr}()$ and determinant $\det()$ are common examples. Invariants are fundamental to DTI analysis because they measure intrinsic diffusive properties, irrespective of the coordinate frame of the acquisition. The gradients of invariants are perpendicular to the orbits, and thus span local variations in tensor shape, the first half of our framework (Section II-A). The tangents to orbits, which we term *rotation tangents*, span local variations in tensor orientation, the second half of our framework (Section II-B).

A. Invariant Gradients

The gradient $\partial J / \partial \mathbf{D}$ of invariant $J : \text{Sym}_3 \mapsto \mathbb{R}$ is a second-order tensor representing the local linear variation of J , used in the first-order Taylor expansion of J around \mathbf{D}_0 [33]

$$J(\mathbf{D}_0 + d\mathbf{D}) = J(\mathbf{D}_0) + \frac{\partial J}{\partial \mathbf{D}}(\mathbf{D}_0) : d\mathbf{D} + O(d\mathbf{D}^2). \quad (6)$$

We use ∇_D to denote the gradient of a function with respect to its tensor-valued argument (while gradients with respect to position in \mathbb{R}^3 are denoted by the usual ∇)

$$\nabla_D J : \text{Sym}_3 \mapsto \text{Sym}_3 \quad (7)$$

$$\nabla_D J \equiv \frac{\partial J}{\partial \mathbf{D}} \quad (8)$$

$$[\nabla_D J]_{ij} = \frac{\partial J}{\partial D_{ij}}. \quad (9)$$

We use “invariant gradient” to refer generally to the gradient of an invariant, rather than to some gradient which is invariant. Formulae for invariant gradients are found by transforming the expression $J(\mathbf{D} + d\mathbf{D})$ into the form of (6) [33]. Two invariants J_1 and J_2 are orthogonal if $\nabla_D J_1(\mathbf{D}) : \nabla_D J_2(\mathbf{D}) = 0$ for all \mathbf{D} . Geometrically, level-sets of two orthogonal invariants are everywhere perpendicular.

Second-order three-dimensional tensors have three independent invariants [46]. There are various ways to parameterize tensor shape with three *orthogonal* invariants. We build on our previous work that advocated two particular sets of three orthogonal invariants, notated K_i and R_i [41]

$$\begin{aligned} K_1(\mathbf{D}) &\equiv \text{tr}(\mathbf{D}) & R_1(\mathbf{D}) &\equiv |\mathbf{D}| \\ K_2(\mathbf{D}) &\equiv |\tilde{\mathbf{D}}| & R_2(\mathbf{D}) &\equiv \text{FA}(\mathbf{D}) \\ K_3(\mathbf{D}) &= R_3(\mathbf{D}) \equiv \text{mode}(\mathbf{D}). \end{aligned} \quad (10)$$

The mode invariant is [47]

$$\text{mode}(\mathbf{D}) \equiv 3\sqrt{6} \det(\tilde{\mathbf{D}}/|\tilde{\mathbf{D}}|). \quad (11)$$

The K_i and R_i invariant sets are analogous to either cylindrical (K_i) or spherical (R_i) coordinate systems for the three-dimensional space of diagonal matrices [41]. We adopt these invariant sets because they naturally isolate biologically significant tensor attributes of size, amount of anisotropy, and type of anisotropy, as described below. Individual eigenvalues also form an orthogonal set, but fail to isolate size and anisotropy. Bahn also described an orthogonal coordinate system of tensor invariants, but used trigonometric functions of eigenvalues rather than standard tensor analysis [48].

In both invariant sets, the first invariant (K_1 or R_1) parameterizes over-all tensor size, in units of diffusivity. K_1 is the trace $\lambda_1 + \lambda_2 + \lambda_3$ (three times bulk mean diffusivity or “ADC”). R_1 is the tensor norm, equal to $\sqrt{\lambda_1^2 + \lambda_2^2 + \lambda_3^2}$. Either K_1 or R_1 readily distinguishes between the cerebral-spinal fluid (CSF) and the brain parenchyma, an important anatomical boundary, because their mean diffusivities differ by a factor of about four [2]. Rapid detection of ischemic stroke is the most common application of diffusion-weighted imaging, based on observing elevated bulk mean diffusivity (that is, changes in K_1) in the parenchyma [11], [12].

The second invariant (K_2 or R_2) parameterizes the amount of anisotropy. K_2 is proportional to the standard deviation of the eigenvalues (with units of diffusivity) [41]. R_2 is the popular fractional anisotropy (FA) measure, which is dimensionless and varies between zero and one [13]. FA is fundamental to DTI applications because differences in diffusive properties attributed to disease (or other biological processes) are so consistently reported in terms of changes in FA [3], [5], [8], [49]–[52]. It is thus appropriate to align one axis of a tensor coordinate system along variation of FA.

The third invariant in both sets $K_3 = R_3$ is termed *mode* by Criscione *et al.* in a continuum mechanics context [47]. Mode is a dimensionless parameter of anisotropy *type*, varying between

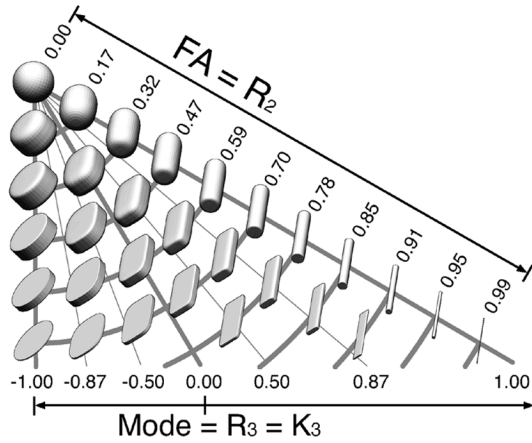


Fig. 1. Illustration of the bivariate space of $FA = R_2$ and $Mode = R_3 = K_3$ for tensors of fixed norm R_1 . The space is properly arranged as a right triangle; this creates orthogonality between the isocontours of FA and $Mode$.

-1 and $+1$, proportional to eigenvalue skewness [41].¹ Negative mode indicates planar anisotropy (oblateness, two large eigenvalues and one small eigenvalue); positive mode indicates linear anisotropy (prolateness, one large eigenvalue and two small). Fig. 1 illustrates the space spanned by tensor mode and FA , using superquadric tensor glyphs [53], [54]. Mode becomes less meaningful when K_2 or R_2 is low.

Tensor mode is significant in at least two contexts. Analysis of DTI partial voluming shows how adjacent regions of linear anisotropy along orthogonal orientations can create planar anisotropy [55], [56]. Planar anisotropy can also arise in populations of differently-oriented fibers mixing at a scale below imaging resolution [57]–[59]. Tensor mode may be more sensitive to noise than other invariants [60], though this also suggests the value of isolating tensor mode in our framework, so that it may be selectively utilized or ignored.

The tensor-valued gradients of K_i and R_i form the first half of our framework. They are derived in [41]

$$\begin{aligned} \nabla_D K_1(\mathbf{D}) &= \mathbf{I} & \nabla_D R_1(\mathbf{D}) &= \mathbf{D}/|\mathbf{D}| \\ \nabla_D K_2(\mathbf{D}) &= \boldsymbol{\Theta}(\mathbf{D}) & \nabla_D R_2(\mathbf{D}) &= \sqrt{\frac{3}{2}} \left(\frac{\boldsymbol{\Theta}(\mathbf{D})}{|\mathbf{D}|} - \frac{|\tilde{\mathbf{D}}| \mathbf{D}}{|\mathbf{D}|^3} \right) \\ \nabla_D K_3(\mathbf{D}) &= \nabla_D R_3(\mathbf{D}) \\ &= \frac{3\sqrt{6}\boldsymbol{\Theta}(\mathbf{D})^2 - 3K_3(\mathbf{D})\boldsymbol{\Theta}(\mathbf{D}) - \sqrt{6}\mathbf{I}}{K_2(\mathbf{D})} \end{aligned} \quad (12)$$

where $\boldsymbol{\Theta}(\mathbf{D}) = \tilde{\mathbf{D}}/|\tilde{\mathbf{D}}|$. Orthogonality was proven in [41]

$$\nabla_D K_1 : \nabla_D K_2 = \nabla_D K_2 : \nabla_D K_3 = \nabla_D K_3 : \nabla_D K_1 = 0 \quad (13)$$

$$\nabla_D R_1 : \nabla_D R_2 = \nabla_D R_2 : \nabla_D R_3 = \nabla_D R_3 : \nabla_D R_1 = 0. \quad (14)$$

Note that $\nabla_D \text{tr} : \nabla_D FA = \nabla_D K_1 : \nabla_D R_2 \neq 0$ [41]. That is, the two most popular invariants, bulk mean diffusivity

¹Skewness is the third standardized moment μ_3/σ^3 , where μ_3 is the third central moment and $\sigma = \sqrt{\mu_2}$ is the standard deviation. In the DTI literature, however, skewness sometimes refers to μ_3 .

(“ADC”) and FA , are not orthogonal measures, despite their frequent paired use. The choice between $\{K_i\}$ and $\{R_i\}$ may depend on the application, though our initial experience suggests that results are similar with either set. Detecting white matter structures in the healthy brain, for example, may benefit from the empirical constancy of bulk mean diffusivity ($K_1/3$) in the parenchyma [2], [60], leaving K_2 and K_3 to capture remaining anisotropy information. If some pathology is indicated by reduced $FA = R_2$, then the $\{R_i\}$ set may be more effective.

To create elements of an orthonormal Sym_3 basis, we always normalize invariant gradients. $\widehat{\nabla}_D J$ denotes the unit-norm tensor-valued gradient of invariant J

$$\widehat{\nabla}_D J(\mathbf{D}) \equiv \nabla_D J(\mathbf{D}) / |\nabla_D J(\mathbf{D})|. \quad (15)$$

A consequence of this normalization for our framework is that invariants are effectively insensitive to changes in parameterization. For example, relative anisotropy (RA) [13] is in fact a monotonic reparameterization of FA [48], which implies $\widehat{\nabla}_D RA(\mathbf{D}) = \widehat{\nabla}_D FA(\mathbf{D})$. The role of an invariant in our framework is thus to parameterize some degree-of-freedom in tensor shape (represented locally by the *direction* of the invariant gradient), while the specifics of that parameterization (encoded in the magnitude of the gradient) are immaterial.

B. Rotation Tangents

In contrast to our definition of invariant gradients (without reference to tensor eigenvalues), the rotation tangents in the second half of our framework are defined explicitly in terms of the tensor eigenvectors $\{\mathbf{e}_1, \mathbf{e}_2, \mathbf{e}_3\}$, due to their importance in DTI applications. In nervous tissue, the principal eigenvector \mathbf{e}_1 is aligned with the direction of the white matter fiber tracts [2], [14], [16], which is the basis of most deterministic fiber tracking algorithms [61], [62].

Let $\mathbf{R}_v(\phi) \in SO_3$ be rotation by angle ϕ around \mathbf{v} . We define the *rotation tangent* $\Phi_i(\mathbf{D})$ associated with eigenvector \mathbf{e}_i of \mathbf{D} as the change in tensor value due to infinitesimal rotations around \mathbf{e}_i . In terms of the group action ψ (4)

$$\Phi_i(\mathbf{D}) \equiv \left. \frac{\partial \psi(\mathbf{R}_{\mathbf{e}_i}(\phi), \mathbf{D})}{\partial \phi} \right|_{\phi=0}. \quad (16)$$

Manipulating matrix representations in the principal frame leads to a coordinate-free expression for $\Phi_1(\mathbf{D})$, as shown in (17) at the bottom of the next page. The other rotation tangents are similarly derived

$$\Phi_2(\mathbf{D}) = (\lambda_1 - \lambda_3)(\mathbf{e}_1 \otimes \mathbf{e}_3 + \mathbf{e}_3 \otimes \mathbf{e}_1) \quad (18)$$

$$\Phi_3(\mathbf{D}) = (\lambda_1 - \lambda_2)(\mathbf{e}_1 \otimes \mathbf{e}_2 + \mathbf{e}_2 \otimes \mathbf{e}_1). \quad (19)$$

Like the eigenvectors with which they are defined, the Φ_i functions have no intrinsic sign. Tensor field measures created with the Φ_i (Sections III-A and III-B) must, therefore, be invariant with respect to the sign of Φ_i .

The rotation tangents $\Phi_i(\mathbf{D})$ are mutually orthogonal, and all $\Phi_i(\mathbf{D})$ are orthogonal to all invariant gradients (see Appendix A). Unit-norm rotation tangents are defined as

$$\widehat{\Phi}_1(\mathbf{D}) \equiv (\mathbf{e}_2 \otimes \mathbf{e}_3 + \mathbf{e}_3 \otimes \mathbf{e}_2)/\sqrt{2} \quad (20)$$

$$\widehat{\Phi}_2(\mathbf{D}) \equiv (\mathbf{e}_3 \otimes \mathbf{e}_1 + \mathbf{e}_1 \otimes \mathbf{e}_3)/\sqrt{2} \quad (21)$$

$$\widehat{\Phi}_3(\mathbf{D}) \equiv (\mathbf{e}_1 \otimes \mathbf{e}_2 + \mathbf{e}_2 \otimes \mathbf{e}_1)/\sqrt{2}. \quad (22)$$

Our framework for tensor analysis is the combination of normalized invariant gradients (either $\{\widehat{\nabla}_D K_i\}$ or $\{\widehat{\nabla}_D R_i\}$) and rotation tangents $\{\widehat{\Phi}_i\}$. The six mutually orthogonal unit-norm tensors constitute an orthonormal Sym_3 basis. Unlike the \mathbf{B} basis in (1), however, our framework decomposes local tensor variations in terms of biologically meaningful attributes. Appendix B describes some subtleties in distinguishing shape and orientation variation near rotationally symmetric tensors.

C. Example Application: Tunable Difference Measures

Although our primary focus is higher-order tensors, we can also decompose discrete tensor differences into shape and rotation components. Measuring large-scale differences between tensor values is a topic addressed in a Riemannian context by numerous authors [39], [63]–[66], although Euclidean differences also have precedent [19], [25]. A common difference measure of \mathbf{D}_1 and \mathbf{D}_2 is the Frobenius norm of the difference, $|\mathbf{D}_1 - \mathbf{D}_2|$, which can also be expressed via projections of $\mathbf{D}_1 - \mathbf{D}_2$ onto the Sym_3 basis, using (3)

$$|\mathbf{D}_1 - \mathbf{D}_2| = \sqrt{\sum_{i=1\dots 6} ((\mathbf{D}_1 - \mathbf{D}_2) : \mathbf{B}_i)^2}.$$

Around the mean $\langle \mathbf{D} \rangle = (\mathbf{D}_1 + \mathbf{D}_2)/2$, invariant gradients $\widehat{\nabla}_D K_i(\langle \mathbf{D} \rangle)$ (or $\widehat{\nabla}_D R_i(\langle \mathbf{D} \rangle)$) and rotation tangents $\widehat{\Phi}_i(\langle \mathbf{D} \rangle)$ form a basis to decompose tensor differences. Similar to the approach of Schultz *et al.* [67], six weights can tune the significance of differences in shape (σ_i) and orientation (ω_i), shown in (23) at the bottom of the page. When $\sigma_i = 1$ and $\omega_i = 1$ for all i then $\text{diff}(\mathbf{D}_1, \mathbf{D}_2) = |\mathbf{D}_1 - \mathbf{D}_2|$. The values of the weights can be determined by the biological context of the processing task. For example, the normalized tensor scalar product (NTSP) measure of Jonasson *et al.* [25] is akin to setting $\sigma_1 = 0$ (and other weights to 1), in that it removes sensitivity to differences in tensor size. Alternatively, the difference measure can be made more robust by tuning the weights according to the noise sensitivity of the tensor parameters, given the experimental design [68]. In any case, we note that because the invariant gradients and rotation tangents are defined locally around the tensor mean, their suitability diminishes as the tensor difference increases.

III. GRADIENT AND COVARIANCE ANALYSIS METHODS

Our framework permits novel decompositions of third-order gradient tensors (Section III-A) and fourth-order covariance tensors (Section III-B). Section III-C reviews spline-based tensor field reconstruction and differentiation. Section III-D describes two datasets designed to illustrate these methods.

A. Third-Order Diffusion Gradient Tensors

Let \mathbf{F} be a smooth tensor-valued image, or tensor field

$$\begin{aligned} \mathbf{F} : \mathbb{R}^3 &\mapsto \text{Sym}_3 \\ \mathbf{F}(\mathbf{x}) &= \mathbf{D} \\ [\mathbf{F}(\mathbf{x})]_{ij} &= D_{ij} \end{aligned} .$$

$$\begin{aligned} [\psi(\mathbf{R}_{\mathbf{e}_1}(\phi), \mathbf{D})]_{\mathcal{E}} &= [\mathbf{R}_{\mathbf{e}_1}(\phi)]_{\mathcal{E}} [\mathbf{D}]_{\mathcal{E}} [\mathbf{R}_{\mathbf{e}_1}(\phi)]_{\mathcal{E}}^{\top} \\ &= \begin{bmatrix} 1 & 0 & 0 \\ 0 & \cos \phi & -\sin \phi \\ 0 & \sin \phi & \cos \phi \end{bmatrix} \begin{bmatrix} \lambda_1 & 0 & 0 \\ 0 & \lambda_2 & 0 \\ 0 & 0 & \lambda_3 \end{bmatrix} \begin{bmatrix} 1 & 0 & 0 \\ 0 & \cos \phi & \sin \phi \\ 0 & -\sin \phi & \cos \phi \end{bmatrix} \\ &= \begin{bmatrix} \lambda_1 & & 0 \\ 0 & \cos^2 \phi \lambda_2 + \sin^2 \phi \lambda_3 & \cos \phi \sin \phi \lambda_2 - \cos \phi \sin \phi \lambda_3 \\ 0 & \cos \phi \sin \phi \lambda_2 - \cos \phi \sin \phi \lambda_3 & \sin^2 \phi \lambda_2 + \cos^2 \phi \lambda_3 \end{bmatrix} \\ &\Rightarrow \left[\frac{\partial \psi(\mathbf{R}_{\mathbf{e}_1}(\phi), \mathbf{D})}{\partial \phi} \Big|_{\phi=0} \right]_{\mathcal{E}} = \begin{bmatrix} 0 & 0 & 0 \\ 0 & 0 & \lambda_2 - \lambda_3 \\ 0 & \lambda_2 - \lambda_3 & 0 \end{bmatrix} \\ &\Rightarrow \Phi_1(\mathbf{D}) = (\lambda_2 - \lambda_3)(\mathbf{e}_2 \otimes \mathbf{e}_3 + \mathbf{e}_3 \otimes \mathbf{e}_2) \end{aligned} \quad (17)$$

$$\text{diff}(\mathbf{D}_1, \mathbf{D}_2) \equiv \sqrt{\sum_{i=1,2,3} \left(\sigma_i (\mathbf{D}_1 - \mathbf{D}_2) : \widehat{\nabla}_D K_i(\langle \mathbf{D} \rangle) \right)^2 + \left(\omega_i (\mathbf{D}_1 - \mathbf{D}_2) : \widehat{\Phi}_i(\langle \mathbf{D} \rangle) \right)^2} \quad (23)$$

The spatial gradient of \mathbf{F} is a third-order tensor [33]

$$\begin{aligned}\nabla\mathbf{F} : \mathbb{R}^3 &\mapsto \text{Sym}_3 \otimes \mathbb{R}^3 \\ \nabla\mathbf{F}(\mathbf{x}) &= \mathcal{G} \\ [\nabla\mathbf{F}(\mathbf{x})]_{ijk} &= \left[\frac{\partial\mathbf{F}(\mathbf{x})}{\partial x_k} \right]_{ij} = \frac{\partial D_{ij}}{\partial x_k} = G_{ijk}.\end{aligned}\quad (24)$$

Spatial gradients of tensor fields were first applied to DTI by Pajevic *et al.*, as part of their spline-based reconstruction [34]. Edges and boundaries in the tensor field may be detected by increases in the over-all gradient magnitude

$$|\nabla\mathbf{F}| = \sqrt{\frac{\partial D_{ij}}{\partial x_k} \frac{\partial D_{ij}}{\partial x_k}}.\quad (25)$$

The tensor field gradient can also be decomposed into the gradients of the isotropic and the deviatoric parts, to measure the magnitude of each separately [34].

Note that given a fixed tensor \mathbf{T} in Sym_3 , the contraction $\mathbf{T} : \mathcal{G}$ is the vector-valued gradient of the scalar $\mathbf{T} : \mathbf{F}(\mathbf{x})$

$$\mathbf{T} : \mathcal{G} = \mathbf{T} : \nabla\mathbf{F}(\mathbf{x}) = \nabla(\mathbf{T} : \mathbf{F}(\mathbf{x})).\quad (26)$$

Thus, contractions of the gradient tensor $\nabla\mathbf{F}$ can access the differential structure of attributes of \mathbf{F} . Invariant gradients and rotation tangents provide the second-order tensors with which we contract $\nabla\mathbf{F}$, generating three spatial gradient vectors of tensor shape, and three spatial gradients of tensor orientation.

The composition $(J \circ \mathbf{F})(\mathbf{x}) = J(\mathbf{F}(\mathbf{x}))$ of tensor field \mathbf{F} and invariant J is a scalar field. With the chain rule

$$\begin{aligned}\nabla J \circ \mathbf{F} : \mathbb{R}^3 &\mapsto \mathbb{R}^3 \\ \nabla J(\mathbf{F}(\mathbf{x})) &= \frac{\partial J}{\partial \mathbf{x}} = \frac{\partial J}{\partial \mathbf{D}} : \frac{\partial \mathbf{D}}{\partial \mathbf{x}} \\ &= \nabla_D J(\mathbf{F}(\mathbf{x})) : \nabla\mathbf{F}(\mathbf{x}) \\ [\nabla J(\mathbf{F}(\mathbf{x}))]_k &= \frac{\partial J}{\partial D_{ij}} \frac{\partial D_{ij}}{\partial x_k}.\end{aligned}\quad (27)$$

Using normalized invariant gradients from the first half of our framework, we define the *projected gradient* of invariant J in tensor field \mathbf{F} as contracting $\nabla\mathbf{F}$ with the unit-norm $\widehat{\nabla}_D J$

$$\begin{aligned}\nabla\widehat{J} : \mathbb{R}^3 &\mapsto \mathbb{R}^3 \\ \nabla\widehat{J}(\mathbf{x}) &\equiv \widehat{\nabla}_D J(\mathbf{F}(\mathbf{x})) : \nabla\mathbf{F}(\mathbf{x}) \\ &= \nabla_D J(\mathbf{F}(\mathbf{x})) : \nabla\mathbf{F}(\mathbf{x}) / |\nabla_D J(\mathbf{F}(\mathbf{x}))| \\ &= \nabla J(\mathbf{F}(\mathbf{x})) / |\nabla_D J(\mathbf{F}(\mathbf{x}))|\end{aligned}\quad (28)$$

$\nabla\widehat{J}$ is an abuse of notation to indicate normalization by tensor norm $|\nabla_D J|$, not vector length $|\nabla J|$; i.e., $\nabla\widehat{J} \neq \widehat{\nabla} J$.

Using the rotation tangents from the second half of our framework, we define three spatial gradients of orientation, one for each of the tensor eigenvectors

$$\begin{aligned}\nabla\widehat{\phi}_i : \mathbb{R}^3 &\mapsto \mathbb{R}^3 \\ \nabla\widehat{\phi}_i(\mathbf{x}) &\equiv \widehat{\Phi}_i(\mathbf{F}(\mathbf{x})) : \nabla\mathbf{F}(\mathbf{x}).\end{aligned}\quad (29)$$

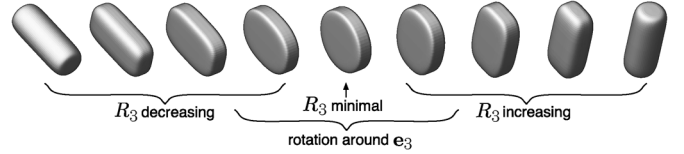


Fig. 2. Continuous variation between linear, planar, and linear anisotropy characterizes interfaces between orthogonally oriented fiber tracts. Together, $\nabla\widehat{R}_3$ and $\nabla\widehat{\phi}_3$ can detect these variations.

Note that $\nabla\widehat{\phi}_i$ is also an abuse of notation: there is no scalar field ϕ_i in which we can measure the spatial gradient. Rather, $\nabla\widehat{\phi}_i$ indicates the direction (in \mathbb{R}^3) along which the tensor orientation “ ϕ_i ” around eigenvector \mathbf{e}_i varies fastest.

Appendix B describes how $\widehat{\nabla}_D R_3$ and $\widehat{\Phi}_3$ become interchangeable near planar anisotropy. This suggests that $|\nabla\widehat{R}_3|$ and $|\nabla\widehat{\phi}_3|$ are complementary gradient measures that could be usefully combined to highlight particular features. Fig. 2 schematically illustrates a configuration that can arise between two adjacent white matter fiber tracts with orthogonal orientation. With the band-limited nature of MRI enforcing some partial voluming of tissue boundaries, this configuration creates intermediate planar anisotropy [55], [56]. As illustrated in Fig. 2, this configuration is characterized by variations in both tensor mode and orientation around the minor eigenvector \mathbf{e}_3 , quantified with $\nabla\widehat{R}_3$ and $\nabla\widehat{\phi}_3$, respectively.

We introduce a measure to detect interfaces of orthogonally oriented anisotropy, called *adjacent orthogonality* (AO)

$$\text{AO}(\mathbf{x}) \equiv \sqrt{|\nabla\widehat{R}_3(\mathbf{x})|^2 + |\nabla\widehat{\phi}_3(\mathbf{x})|^2}.\quad (30)$$

AO responds mostly strongly to interfaces of anisotropy with orthogonal orientation, but any distinct orientation leads to nonzero $|\nabla\widehat{\phi}_3(\mathbf{x})|$, and some AO response. AO is defined and demonstrated herein only with gradient magnitudes, but the $\nabla\widehat{R}_3(\mathbf{x})$ and $\nabla\widehat{\phi}_3(\mathbf{x})$ vectors define the interface orientation.

B. Fourth-Order Diffusion Covariance Tensors

The fourth-order covariance tensor Σ of a set of second-order tensors $\{\mathbf{D}_i\}$ is a compact description of the shape of the distribution of \mathbf{D}_i . Fourth-order tensors can be understood by analogy to second-order tensor products of vectors. Recall (Table I) that the tensor product $\mathbf{u} \otimes \mathbf{v}$ of two vectors \mathbf{u} and \mathbf{v} is a second-order tensor in $\mathbb{R}^3 \otimes \mathbb{R}^3$ for which $[\mathbf{u} \otimes \mathbf{v}]_{ij} = u_i v_j$. Similarly, for tensors \mathbf{U} and \mathbf{V} in Sym_3 , the tensor product $\mathbf{U} \otimes \mathbf{V}$ is a fourth-order tensor in $\text{Sym}_3 \otimes \text{Sym}_3$ for which $[\mathbf{U} \otimes \mathbf{V}]_{ijkl} = U_{ij} V_{kl}$. The diffusion covariance tensor Σ is a weighted sum of tensor products of tensors from the set $\{\mathbf{D}_i\}$

$$\Sigma = \sum_{i=1..n} w_i (\mathbf{D}_i - \langle \mathbf{D} \rangle) \otimes (\mathbf{D}_i - \langle \mathbf{D} \rangle)\quad (31)$$

where $\langle \mathbf{D} \rangle = (1/n) \sum_{i=1..n} \mathbf{D}_i$ and $\sum_{i=1..n} w_i = 1$. We use covariance tensors here to summarize a weighted set of given tensors, rather than to parametrically model a continuous distribution [38], or to generate new tensor samples [39].

Building on elasticity methods of continuum mechanics [46], Bassler and Pajevic model distributions of tensors from noisy DWIs with fourth-order covariance tensors, to characterize diffusion-weighted imaging (DWI) experimental design [37]. More recent work assesses covariance tensor structure with spectral decomposition, and quantifies and visualizes the variance of mean diffusivity [38]. Given a noise model for DWIs, the experimental design, and a tensor estimation method, accurately calculating the fourth-order covariance tensor is a central problem in error propagation analysis in DTI, recently studied in the context of weighted linear least-squares tensor estimation [68]. Related work estimates tensor variability according to the Hessian of the objective function minimized in nonlinear least-squares tensor estimation [69]. Other work focuses on determining (without the fourth-order covariance tensor Σ) the variances of the tensor eigenvalues [70], shape invariants [71], or the full eigensystem [72], from which variances of other tensor attributes (such as FA) are computed.

Our preliminary work in covariance tensor analysis is based upon the recognition that *assuming* the covariance tensor Σ is known, some of its important properties can be isolated simply by expressing it in the Sym_3 basis from our framework. Some details of tensor contraction are first reviewed. Analogous to the scalar contraction $\mathbf{u} \cdot \mathbf{D}\mathbf{v} = u_i D_{ij} v_j$ of a second-order tensor \mathbf{D} with vectors \mathbf{u} and \mathbf{v} , the double contraction of a fourth-order tensor \mathbf{S} with second-order tensors \mathbf{U} and \mathbf{V} is $\mathbf{U} : \mathbf{S} : \mathbf{V} = U_{ij} S_{ijkl} V_{kl}$. Contraction determines the individual coefficients of \mathbf{S} given a basis $\mathcal{B} = \{\mathbf{b}_i\}_{i=1,2,3}$ for \mathbb{R}^3

$$S_{ijkl} = ([\mathbf{S}]_{\mathcal{B}})_{ijkl} = (\mathbf{b}_i \otimes \mathbf{b}_j) : \mathbf{S} : (\mathbf{b}_k \otimes \mathbf{b}_l). \quad (32)$$

By the symmetry of Sym_3 , for \mathbf{S} in $\text{Sym}_3 \otimes \text{Sym}_3$ we have

$$S_{ijkl} = S_{jikl} = S_{jilk} = S_{ijlk}. \quad (33)$$

However, knowing that Sym_3 is itself a six-dimensional vector space (Section II), we can more directly define the coefficients of \mathbf{S} relative to a Sym_3 basis, such as \mathcal{B} defined in (1)

$$S_{ij} = ([\mathbf{S}]_{\mathcal{B}})_{ij} = \mathbf{B}_i : \mathbf{S} : \mathbf{B}_j. \quad (34)$$

Recall (Section II) that we use bold subscripts for indices relative to a basis for Sym_3 , rather than for \mathbb{R}^3 . Fourth-order tensors in $\text{Sym}_3 \otimes \text{Sym}_3$ can thus be represented as 6×6 matrices. The various $\sqrt{2}$ and 2 scalings involved in converting from $([\mathbf{S}]_{\mathcal{B}})_{ijkl}$ to $([\mathbf{S}]_{\mathcal{B}})_{ij}$ (fully detailed in [38]) are an automatic consequence of (34) and the \mathcal{B} definition, as were the $\sqrt{2}$ scalings in converting between D_{ij} and \mathbf{D}_i in (2). As a linear combination of symmetric tensor products (31), Σ also has the symmetry [in addition to that of (33)]

$$\Sigma_{ij} = \Sigma_{ji}. \quad (35)$$

Thus, Σ is represented by a symmetric 6×6 matrix, with 21 degrees-of-freedom.

We express the covariance tensor Σ in a Sym_3 basis at $\langle \mathbf{D} \rangle$ generated by our framework

$$\begin{aligned} \mathcal{A}_K(\langle \mathbf{D} \rangle) &= \{\mathbf{A}_i\}_{i=1\dots 6} \\ &\equiv \left\{ \widehat{\nabla}_D K_1(\langle \mathbf{D} \rangle), \widehat{\nabla}_D K_2(\langle \mathbf{D} \rangle), \widehat{\nabla}_D K_3(\langle \mathbf{D} \rangle) \right. \\ &\quad \left. \widehat{\Phi}_1(\langle \mathbf{D} \rangle), \widehat{\Phi}_2(\langle \mathbf{D} \rangle), \widehat{\Phi}_3(\langle \mathbf{D} \rangle) \right\}. \end{aligned} \quad (36)$$

Basis \mathcal{A}_R is similarly defined with the R_i invariant gradients. We stress that these Sym_3 bases are defined around the mean $\langle \mathbf{D} \rangle$ for *each* distribution $\{\mathbf{D}_i\}$. Individual components of the covariance matrix are then [compare to (34)]

$$\Sigma_{ij} = ([\Sigma]_{\mathcal{A}_K(\langle \mathbf{D} \rangle)})_{ij} = \mathbf{A}_i : \Sigma : \mathbf{A}_j. \quad (37)$$

The Sym_3 basis from our framework naturally isolates salient properties of the $\{\mathbf{D}_i\}$ distribution, in that the Σ_{ij} components measure the variances ($i = j$) and covariances ($i \neq j$) of all possible shape and orientation parameters. In particular, certain covariance tensor components directly estimate the variance of parameters such as FA. This is based on the Taylor expansion (6) of J around $\langle \mathbf{D} \rangle$:

$$\begin{aligned} \langle J(\mathbf{D}_i) \rangle &\approx \langle J(\langle \mathbf{D} \rangle) + \nabla_D J(\langle \mathbf{D} \rangle) : (\mathbf{D}_i - \langle \mathbf{D} \rangle) \rangle \\ &= J(\langle \mathbf{D} \rangle) + \nabla_D J(\langle \mathbf{D} \rangle) : \langle \mathbf{D}_i - \langle \mathbf{D} \rangle \rangle \\ &= J(\langle \mathbf{D} \rangle). \end{aligned} \quad (38)$$

Then, contracting the covariance tensor Σ of $\{\mathbf{D}_i\}$ with invariant gradient $\nabla_D J$ approximates the variance of $\{J(\mathbf{D}_i)\}$

$$\begin{aligned} \text{Var}(J(\mathbf{D}_i)) &= \frac{1}{n-1} \sum_i (J(\mathbf{D}_i) - \langle J(\mathbf{D}_i) \rangle)^2 \\ &\approx \frac{1}{n-1} \sum_i (J(\mathbf{D}_i) - J(\langle \mathbf{D} \rangle))^2 \\ &\approx \frac{1}{n-1} \sum_i (\nabla_D J(\langle \mathbf{D} \rangle) : (\mathbf{D}_i - \langle \mathbf{D} \rangle))^2 \\ &= \nabla_D J(\langle \mathbf{D} \rangle) : \Sigma : \nabla_D J(\langle \mathbf{D} \rangle). \end{aligned} \quad (39)$$

In the \mathcal{A}_R basis, the covariance tensor component Σ_{22} approximates the variance of standard anisotropy measures

$$\begin{aligned} \text{Var}(\text{FA}(\mathbf{D}_i)) &\approx \nabla_D \text{FA}(\langle \mathbf{D} \rangle) : \Sigma : \nabla_D \text{FA}(\langle \mathbf{D} \rangle) \\ &= \widehat{\nabla}_D R_2(\langle \mathbf{D} \rangle) : \Sigma : \widehat{\nabla}_D R_2(\langle \mathbf{D} \rangle) \\ &\quad \times |\nabla_D \text{FA}(\langle \mathbf{D} \rangle)|^2 \\ &= \Sigma_{22} |\nabla_D \text{FA}(\langle \mathbf{D} \rangle)|^2 \end{aligned} \quad (40)$$

$$\text{Var}(\text{RA}(\mathbf{D}_i)) \approx \Sigma_{22} |\nabla_D \text{RA}(\langle \mathbf{D} \rangle)|^2. \quad (41)$$

Our framework organizes analysis along degrees-of-freedom parameterized by invariants (represented by $\widehat{\nabla}_D J$), while factoring out the parameterization rate (represented by $|\nabla_D J|$). Thus, the same covariance component Σ_{22} underlies the approximate variance of both RA (40) and FA (41). Contracting Σ along invariant gradient $\nabla_D J$ to estimate the variance of

an arbitrary J generalizes previous covariance tensor analysis that focuses on the variance of ADC ($K_1/3$) [38], and is more straightforward than using the covariance tensor to find the variances of individual eigenvalues, from which variances of invariants (such as RA and FA) are then determined [68].

We can further decompose the fourth-order covariance tensor into novel aggregate measures of overall shape variance σ_{ss} , orientation variance σ_{oo} , as well as shape and orientation covariance σ_{so} , defined as follows:

$$\sigma_{ss} = \sqrt{\sum_{i,j=1,2,3} \Sigma_{ij}^2} \quad (42)$$

$$\sigma_{oo} = \sqrt{\sum_{i,j=4,5,6} \Sigma_{ij}^2} \quad (43)$$

$$\sigma_{so} = \sqrt{\sum_{\substack{i=1,2,3 \\ j=4,5,6}} 2\Sigma_{ij}^2} \quad (44)$$

The covariance components Σ_{ij} can be measured in either the \mathcal{A}_K or the \mathcal{A}_R basis from (36). The aggregate covariance measures maintain total covariance magnitude as

$$\sqrt{\sigma_{ss}^2 + \sigma_{oo}^2 + \sigma_{so}^2} = |\Sigma| = \sqrt{\Sigma_{ij}\Sigma_{ij}} \quad (45)$$

C. Convolution-Based Reconstruction and Differentiation

We adopt the B -spline tensor interpolation method of Pajevic *et al.* [34], [73], briefly reviewed here. The interpolation creates a continuous and differentiable tensor field $\mathbf{F}(\mathbf{x})$ by convolving discrete tensor samples with the separable uniform cubic B -spline kernel $B(x, y, z) = b(x)b(y)b(z)$, where

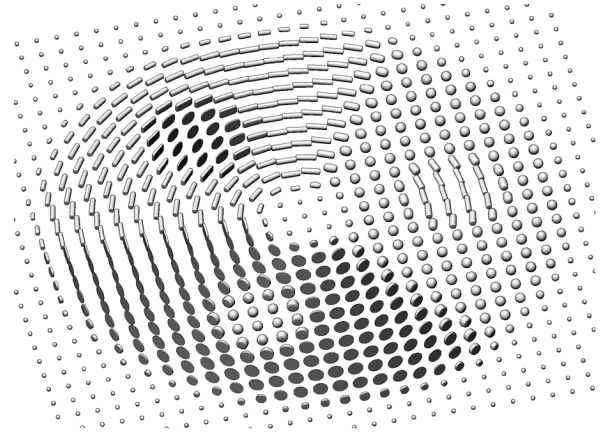
$$b(x) = \begin{cases} 0 & |x| > 2 \\ -(|x| - 2)^3/6 & 1 < |x| < 2 \\ (|x| - 2)|x|^2/2 + 2/3 & 0 < |x| < 1 \end{cases} \quad (46)$$

The tensors samples are prefiltered per-component (in the \mathbb{R}^3 basis of the scanner), so that subsequent convolution with $B(x, y, z)$ interpolates through the tensors originally estimated from the DWIs [74], [75]. By the linearity of convolution and differentiation, the partial derivatives of the reconstructed tensor field $\mathbf{F}(\mathbf{x})$ are found by convolving with the partial derivatives of $B(x, y, z)$. The reconstructed values and gradients can be computed at arbitrary locations in the field by evaluating $B(x, y, z)$ (or its partial derivatives) to determine weights for corresponding tensor sample locations, within the $4 \times 4 \times 4$ sample support of the kernel.

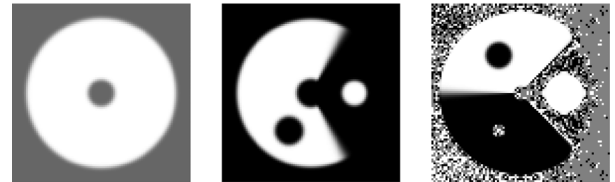
D. Synthetic Datasets

Carefully designed synthetic datasets help illustrate the behavior of our tensor analysis methods, and give insight into their potential applications. We describe two datasets that exhibit particular features in tensor shape and orientation.

Fig. 3 depicts a synthetic tensor image constructed to demonstrate edge detection with invariant gradients K_i . There are four distinct materials: isotropic with low diffusivity, isotropic with



(a) Glyph rendering of downsampled synthetic data



(b) K_1

(c) K_2

(d) K_3

Fig. 3. Synthetic data with tensor shape boundaries. Glyph rendering (of downsampled data) in (a) shows the variety of size, anisotropy, and orientation; (b), (d), (d) show the K_i invariants. K_3 is essentially noise when K_2 is at or near zero (regardless of the value of K_1); the important structure of K_3 in (d) is the contrast between low and high values of K_3 where K_2 is high. (a) Glyph rendering of downsampled synthetic data; (b) K_1 ; (c) K_2 ; (d) K_3 .

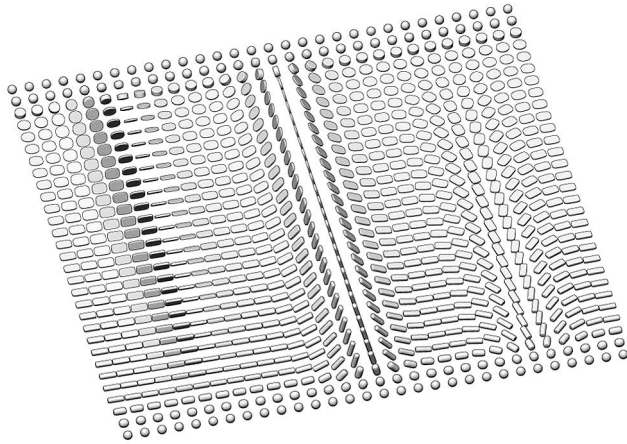
high diffusivity, linear anisotropic, and planar anisotropic. As seen in Fig. 3(a), the orientation of the tensors also changes smoothly within the anisotropic regions. Interfaces exist between every pair of materials.

Fig. 4 depicts a synthetic tensor image with gradients in tensor orientation. The image is divided horizontally into three regions of rotation, one for each eigenvector. Fig. 4(a) renders the dataset with glyphs. The glyphs illustrate an implication of (17)–(19): the effect of rotation on a tensor is modulated by its symmetries (e.g., rotation around \mathbf{e}_1 has no effect when $\lambda_2 = \lambda_3$). Eigenvalue mean K_1 is held constant throughout the image, and variance K_2 is constant except for isotropic bands at the top and bottom. Tensor mode K_3 varies smoothly from top to bottom, covering the full range from planar to linear anisotropy.

IV. RESULTS

Section IV-A presents our results in third-order gradient tensor analysis, and Section IV-B gives fourth-order tensor analysis results. Examples use either the K_i or R_i invariants, but both produce similar results. After Fig. 5, all grayscale images are inverted for visual clarity.

Besides the synthetic datasets described above, results are also shown with a DTI scan of a healthy human volunteer. Single-shot EPI diffusion-weighted images (DWIs) along 30 gradient directions ($b = 700 \text{ s/mm}^2$), and five nondiffusion-weighted images, were acquired on a 1.5-T Philips scanner with parallel imaging (SENSE factor 2.5). The field-of-view, size of the acquisition matrix, and slice thickness are 240 mm



(a) Glyph rendering of downsampled synthetic data

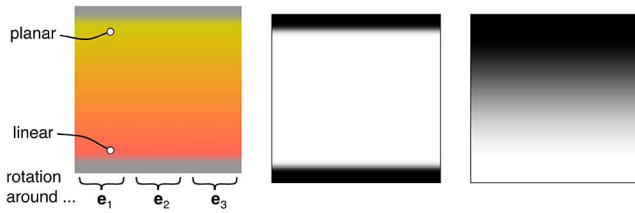
(b) Synthetic image layout; $(\lambda_1, \lambda_2, \lambda_3)$ triples shown by RGB color(c) K_2 (d) K_3

Fig. 4. Synthetic data with tensor orientation boundaries. Glyphs in (a) show the range of anisotropy type and the three regions of rotation, as diagrammed in (b). (c) and (d) show K_2 and K_3 ; K_1 is constant. (a) Glyph rendering of downsampled synthetic data; (b) synthetic image layout; $(\lambda_1, \lambda_2, \lambda_3)$ triples shown by RGB color; (c) K_2 ; (d) K_3 .

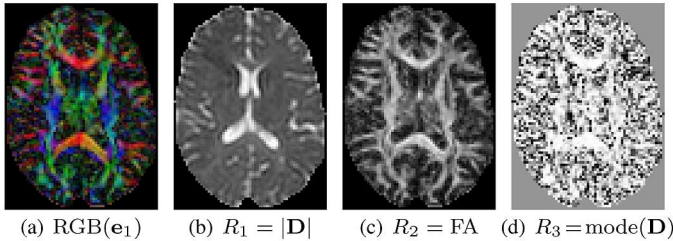
(a) RGB(\mathbf{e}_1) (b) $R_1 = |\mathbf{D}|$ (c) $R_2 = \text{FA}$ (d) $R_3 = \text{mode}(\mathbf{D})$

Fig. 5. Slice of scan of healthy volunteer, shown with principal eigenvector colormap (a), and the R_i invariants (b), (c), and (d), for which the numerical ranges are $[0, 0.006] \times \text{mm}^2/\text{s}$, $[0, 1]$, and $[-1, 1]$, respectively. Image pixels correspond one-to-one with DTI volume samples. The map of tensor mode (d) appears noisy because mode is not well-defined in isotropic regions. (a) RGB(\mathbf{e}_1); (b) $R_1 = |\mathbf{D}|$; (c) $R_2 = \text{FA}$; (d) $R_3 = \text{mode}(\mathbf{D})$.

$\times 240$ mm, 96×96 , and 2.5 mm, respectively. In-plane resolution was zero-fill interpolated to 128×128 . Tensors were fit by linear least-squares to logarithms of DWIs [1]. Fig. 5 shows an axial slice of the data with maps of the principal eigenvector [76] and the R_i invariants. The units of diffusivity (mm^2/s) determine the units of gradient strength in Section IV-A (diffusivity over length, mm/s) and covariance in Section IV-B (diffusivity squared, mm^4/s^2).

A. Gradient Tensor Results

Fig. 6 shows gradient magnitudes in the first synthetic dataset of Section III-D. Previous work decomposes the tensor field gra-

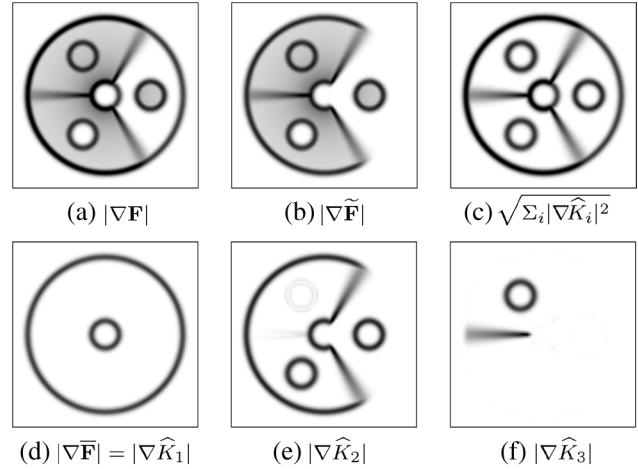


Fig. 6. Gradient magnitudes in first synthetic image. Previous work [34] detects the deviatoric gradient magnitude (b). Our framework isolates boundaries in shape (c), as well as in diffusivity (d), amount of anisotropy (e), and type of anisotropy (f). Numerical ranges on all images are equal. (a) $|\nabla \mathbf{F}|$; (b) $|\nabla \tilde{\mathbf{F}}|$; (c) $\sqrt{\sum_i |\nabla \hat{K}_i|^2}$; (d) $|\nabla \bar{\mathbf{F}}| = |\nabla \hat{K}_1|$; (e) $|\nabla \hat{K}_2|$; (f) $|\nabla \hat{K}_3|$.

dient $\nabla \mathbf{F}$ into gradients of the deviatoric $\nabla \tilde{\mathbf{F}}$ and isotropic $\nabla \bar{\mathbf{F}}$ components [34]. However, $\nabla \mathbf{F}$ and $\nabla \tilde{\mathbf{F}}$ respond to changes in both orientation and shape, manifested by a smooth gray level in the anisotropic material interiors in Fig. 6(a) and (b). Our framework detects shape change independently of orientation change [Fig. 6(c)], and decomposes shape change according to mean diffusivity [Fig. 6(d)], amount of anisotropy [Fig. 6(e)], and type of anisotropy [Fig. 6(f)]. Isolating different boundaries in tensor shape, in terms of biologically meaningful quantities (the K_i or R_i invariants), while excluding variations in orientation, has not been previously described.

Fig. 7 shows gradient magnitudes in the second synthetic dataset. Both shape and orientation changes contribute to $|\nabla \mathbf{F}|$ in Fig. 7(a), and shape changes are decomposed into $|\nabla \hat{K}_2|$ and $|\nabla \hat{K}_3|$ in Fig. 7(b) and (c). Fig. 7(d)–(f) illustrates how $|\nabla \hat{\phi}_1|$, $|\nabla \hat{\phi}_2|$, and $|\nabla \hat{\phi}_3|$ successfully isolate rotations around the individual eigenvectors. This selectivity is not possible with previous analyses of the tensor field gradient. Note that $|\nabla \hat{\phi}_i|$ smoothly decreases with increasing symmetry around eigenvector \mathbf{e}_i , which is not captured by direct measurements of eigenvector angles.

Although not used elsewhere in this work, a consequence of (27) and our $\nabla \mathbf{F}$ measurement (Section III-C) is the ability to *analytically* compute the gradient ∇J of an invariant J in the *continuous* tensor field. For non-linear invariants such as FA, this can differ significantly from pre-computing a scalar field of the invariant values, and then measuring gradients. Fig. 8 demonstrates analytic gradient measurements of the R_i invariants. The $|\nabla R_1|$ image shows ringing (false edges) around the ventricles, perhaps the response of the scanner's zero-fill interpolation to the large change in diffusivity (and hence the DWI value) between CSF and parenchyma.

Fig. 9 demonstrates in acquired DTI data the gradient tensor analysis with our framework. From the decomposition of the total gradient magnitude $|\nabla \mathbf{F}|$ [Fig. 9(a)] into all shape gradients [Fig. 9(b)] and all orientation gradients [Fig. 9(c)], we see

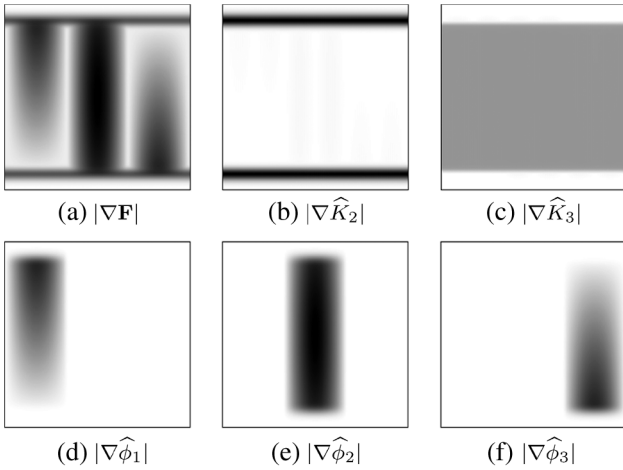


Fig. 7 Gradient magnitudes in second synthetic tensor image. The three different bands in (d), (e), and (f) indicate how the $|\nabla\hat{\phi}_i|$ isolates different changes in orientation. Numerical ranges for (a), (d), (e), and (f) are equal. (a) $|\nabla\mathbf{F}|$; (b) $|\nabla\hat{K}_2|$; (c) $|\nabla\hat{K}_3|$; (d) $|\nabla\hat{\phi}_1|$; (e) $|\nabla\hat{\phi}_2|$; (f) $|\nabla\hat{\phi}_3|$.

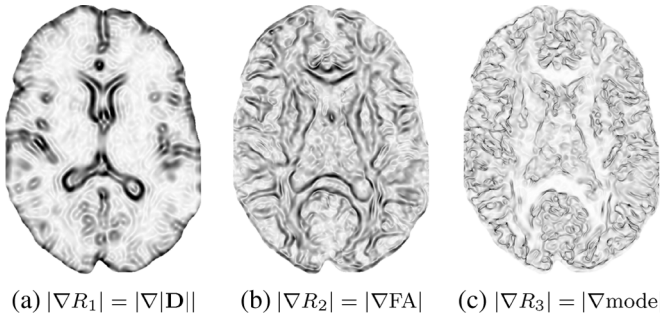


Fig. 8. Analytic evaluation of ∇R_i in the continuous tensor field, sampled at eight times the original data resolution. Numerical ranges for (a), (b), and (c) are $[0, 0.0015]$ mm/s, $[0, 0.35]$ mm⁻¹, and $[0, 8]$ mm⁻¹, respectively. (a) $|\nabla R_1| = |\nabla|\mathbf{D}||$; (b) $|\nabla R_2| = |\nabla\text{FA}|$; (c) $|\nabla R_3| = |\nabla\text{mode}|$.

that the shape gradients contribute more than the orientation gradients to the total magnitude, especially at the ventricle (CSF) boundary. Fig. 9(d) reveals that the CSF edge is well delineated by $|\nabla\hat{R}_1|$, and that variations in R_1 dominate the other shape gradients. Low $|\nabla\hat{R}_1|$ values inside the parenchyma confirm that tensor norm $|\mathbf{D}| = R_1$ is fairly constant across white and gray matter, mirroring known behavior of bulk mean diffusivity ($K_1/3$) [2], [60]. The other edge measure of obvious anatomic significance is $|\nabla\hat{R}_2| = |\nabla\text{FA}|$ in Fig. 9(e), similar to $|\nabla\text{FA}|$ in Fig. 8(b). The difference is that Fig. 8(b) depicts the gradient of a particular invariant, FA, whereas Fig. 9(e) more generally depicts the component of the tensor gradient $\nabla\mathbf{F}$ aligned with variations in FA, or any other invariant parameterizing the same degree-of-freedom (e.g., RA).

The gradient magnitudes along the first two rotation tangents, $\nabla\hat{\phi}_1$ [Fig. 9(g)] and $\nabla\hat{\phi}_2$ [Fig. 9(h)], lack similarly obvious anatomical significance. This suggests either removing these components of the third-order gradient tensor to increase its anatomic specificity, or isolating them as indicators of tensor field noise. Also, the reliance of these measures on sorted eigenvalues (unlike the invariant gradients), combined with noise-induced sorting bias, may disrupt the depiction of underlying coherent patterns of orientation change. Space here does not

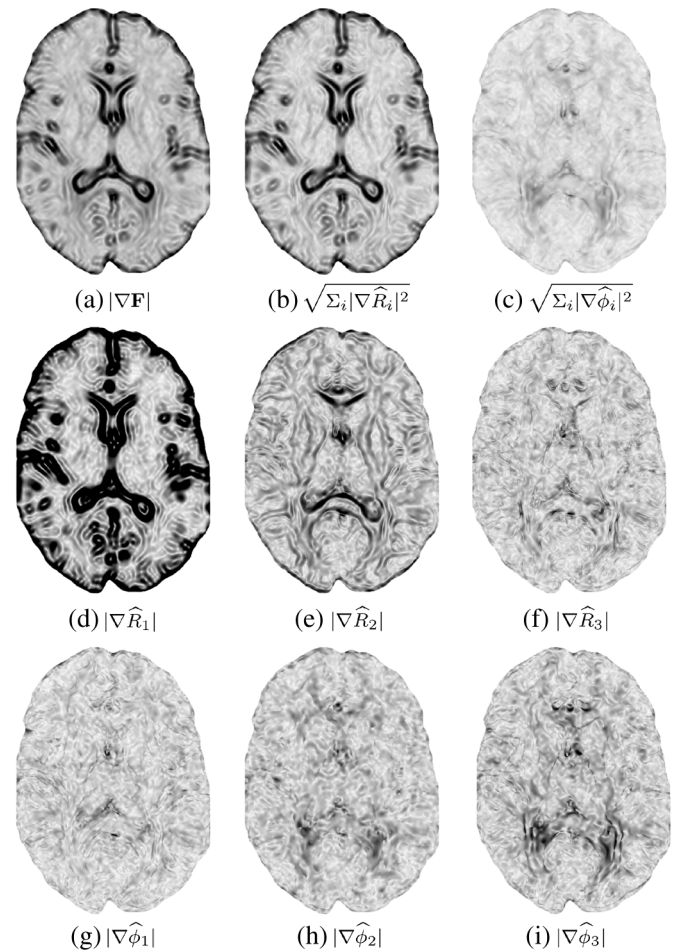


Fig. 9. Decomposition of $|\nabla\mathbf{F}|$ along invariant gradients and rotation tangents. (a) through (c) have numerical range $[0, 1.4] \times 10^{-3}$ mm/s; better visual contrast for (d) through (i) is given by a smaller range $[0, 0.58] \times 10^{-3}$ mm/s. (a) $|\nabla\mathbf{F}|$; (b) $\sqrt{\sum_i |\nabla\hat{R}_i|^2}$; (c) $\sqrt{\sum_i |\nabla\hat{\phi}_i|^2}$; (d) $|\nabla\hat{R}_1|$; (e) $|\nabla\hat{R}_2|$; (f) $|\nabla\hat{R}_3|$; (g) $|\nabla\hat{\phi}_1|$; (h) $|\nabla\hat{\phi}_2|$; (i) $|\nabla\hat{\phi}_3|$.

permit a comparison, but for some purposes it may be better to measure $\nabla\hat{\phi}_i(\mathbf{x}) = \hat{\Phi}_i(\mathbf{F}(\mathbf{x})) : \nabla\mathbf{F}(\mathbf{x})$ rather than $\nabla\hat{\phi}_i$, because implicit in the pair-wise eigenvalue differences [in the $\hat{\Phi}_i$ definition in (17), -(19)] is an anisotropy measure that may usefully mask out isotropic areas.

On the other hand, the complementary structure of $\nabla\hat{R}_3$ [Fig. 9(f)] and $\nabla\hat{\phi}_3$ [Fig. 9(i)] contribute to the AO measure (Section III-A), illustrated in Fig. 10. The RGB colormap [Fig. 10(a)] of the principal diffusion direction depicts multiple sites of adjacency between distinctly or orthogonally oriented fiber tracts. Two such locations are highlighted, between the corpus callosum and cingulum bundle, and in the sequential arrangement of the tapetum of the corpus callosum, the posterior corona radiata, and the superior longitudinal fasciculus [77]. Both $|\nabla\hat{R}_3|$ [Fig. 10(b)] and $|\nabla\hat{\phi}_3|$ [Fig. 10(c)] respond to these interfaces, but each has discontinuities. By combining $|\nabla\hat{R}_3|$ and $|\nabla\hat{\phi}_3|$, AO (Fig. 10(d)) successfully delineates the interfaces between tracts in the indicated regions. Note that these tissue configurations cannot be described in terms of tensor shape or orientation alone. Tensor invariant gradients detect boundaries between different materials, and tensor

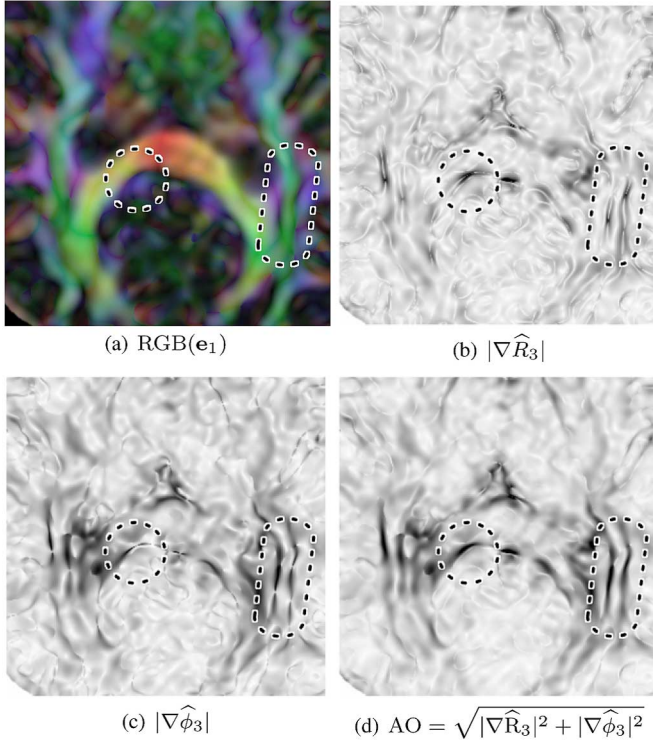


Fig. 10. Adjacent Orthogonality (AO) detects interfaces between orthogonally oriented tracts. The highlighted regions in the $\text{RGB}(\mathbf{e}_1)$ map (a) are the interface between the corpus callosum (red) and cingulum bundle (blue), indicated with the circle, and between the tapetum (purple), posterior corona radiata (green), and superior longitudinal fasciculus (blue), indicated with the box on the right. Each of $|\nabla \hat{R}_3|$ (b) and $|\nabla \hat{\phi}_3|$ (c) detect such configurations to some extent, but AO (d) has more consistent response. (b), (c), and (d) use numerical range $[0, 0.58] \times 10^{-3}$ mm/s.

$ \nabla \hat{R}_1 $	$ \nabla \hat{R}_2 $	$ \nabla \hat{R}_3 $	$ \nabla \hat{\phi}_1 $	$ \nabla \hat{\phi}_2 $	$ \nabla \hat{\phi}_3 $
0.390	0.163	0.109	0.096	0.114	0.127
0.662			0.337		

Fig. 11. Relative magnitudes of spatial gradients of shape ($|\nabla \hat{R}_i|$) and orientation ($|\nabla \hat{\phi}_i|$), after averaging over DTI brain dataset, and relative magnitudes of all shape versus orientation gradients.

eigenvectors can detect anisotropy orientation. Our framework puts shape and orientation into a common coordinate frame, allowing functions like AO to draw on both, delineating white matter regions that internally have comparable anisotropy characteristics.

Fig. 11 gives quantitative information about the relative magnitudes of the gradients mapped in Fig. 9. The numbers were computed by sampling the spatial gradients of shape ($\nabla \hat{R}_i$) and orientation ($\nabla \hat{\phi}_i$) throughout the brain DTI dataset (used previously) at three times data resolution, averaging the gradient norms over the field, and then normalizing. On average, the gradient of $R_1 = |\mathbf{D}|$ accounts for about 40% of gradient tensor magnitude, the gradient of $R_2 = \text{FA}$ is about 16%, and the other gradients were all about 10%. The shape and orientation gradients account for about two thirds and one third of the total gradient strength, respectively. These statistics quantify the relative magnitudes visualized in Fig. 9. Also, as discussed in Section V-A, this type of summary information can inform how our framework is applied to DTI analysis.

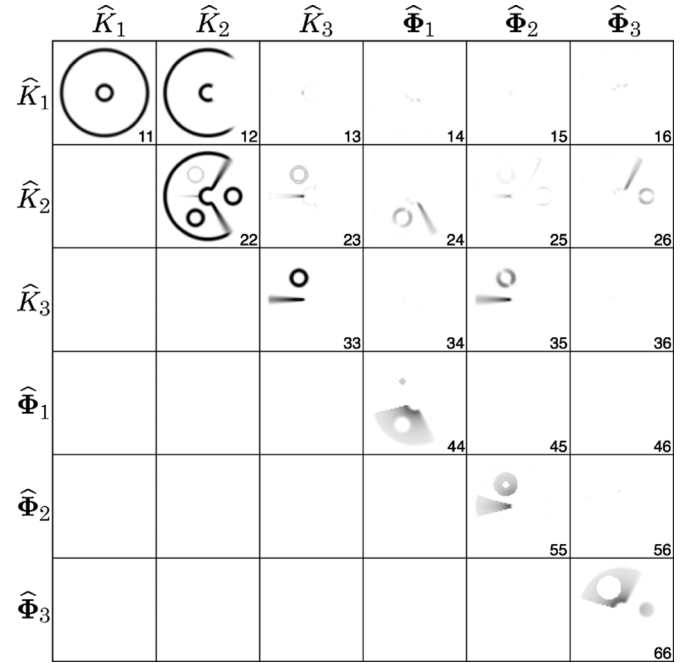


Fig. 12. Matrix of images of components Σ_{ij} of covariance tensor Σ , using the local \mathcal{A}_K basis. Components are identified by basis tensors across the top and left side. Numerical ranges on all components are equal.

B. Covariance Tensor Results

We first analyze covariance tensors with pixel neighborhoods from DTI datasets, to illustrate the basic properties of our covariance tensor decomposition, and to explore the novel metrics σ_{oo} , σ_{ss} , and σ_{so} . Covariance matrices are computed over $3 \times 3 \times 3$ sample neighborhoods, weighted by the (noninterpolating) cubic B -spline (46). Fig. 12 displays the covariance tensor components in the first synthetic dataset. For simplicity, only the absolute value of the components is shown; the rotation tangent components have ambiguous sign. We believe this is the first visual depiction of a field of fourth-order diffusion covariance tensors. The variances (along the diagonal) of the K_i invariants agree with edge measures seen in Fig. 6, but the off-diagonal elements show additional structure. $\Sigma_{12} = \widehat{\nabla}_D K_1 : \Sigma : \widehat{\nabla}_D K_2$, for example, highlights points where eigenvalue mean K_1 and variance K_2 co-vary, as confirmed by Fig. 3(a). Likewise, $\Sigma_{35} = \widehat{\nabla}_D K_3 : \Sigma : \hat{\Phi}_2$ highlights points where K_3 co-varies with rotation around eigenvector \mathbf{e}_2 . The rotation variances Σ_{44} , Σ_{55} , and Σ_{66} indicate continuous orientation change. The individual covariance components are combined to form the aggregate covariance measures σ_{ss} , σ_{oo} , and σ_{so} , illustrated in Fig. 13. The map of σ_{so} [Fig. 13(c)], for example, displays all locations where tensor shape and orientation co-vary.

Fig. 14 measures covariance tensors (with the R_i invariants) in the DTI slice used for previous figures, although to improve resolution, the data was up-sampled (Section III-C) by a factor of three in each axis. The images are not as clean as with the synthetic data, but some results are worth noting. The on-diagonal elements Σ_{11} and Σ_{22} generally agree with the images of the gradient magnitudes of R_1 and R_2 in Fig. 8, which highlight the border between parenchyma and CSF, and the border

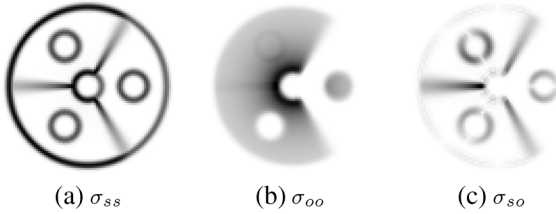


Fig. 13. Shape variance σ_{ss} (a), orientation variance σ_{oo} (b), and shape and orientation covariance σ_{so} (c) evaluated on synthetic data. Comparison to Fig. 3. implies the functions are indeed measuring what their names suggest.

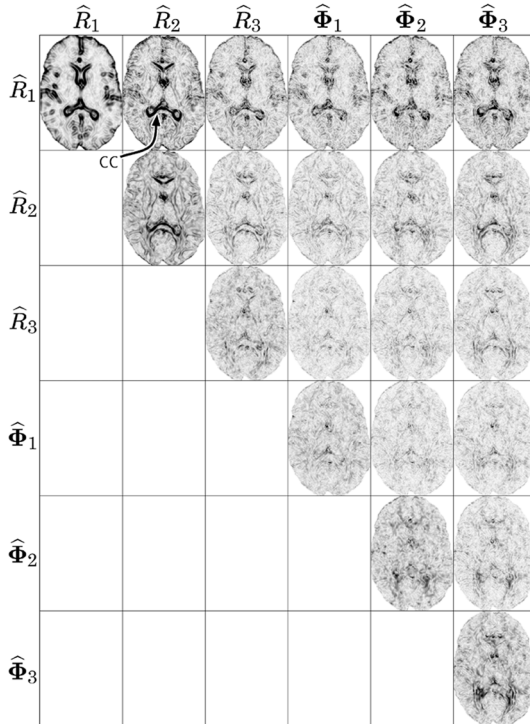


Fig. 14. Covariance tensors measured in DTI data slice, displayed using same layout as in Fig. 12. “CC” annotation in Σ_{12} points to the boundary highlighted between CSF and corpus callosum, where R_1 and R_2 do co-vary. Numerical range of Σ_{11} is $[0, 5.6] \times 10^{-9} \text{ mm}^4/\text{s}^2$, range for all other components is $[0, 1.4] \times 10^{-9} \text{ mm}^4/\text{s}^2$.

between white and gray matter, respectively. The “CC” annotation in the Σ_{12} image points out the boundary of white matter and CSF in the corpus callosum, a location where diffusivity R_1 and anisotropy R_2 should in fact co-vary.

The aggregate covariance measures in Fig. 15 reveal other structural properties. Shape variance σ_{ss} [Fig. 15(a)] shows the major tissue boundaries (black line between CSF and parenchyma, light gray borders between white and gray matter), similar to the analogous quantity from the gradient, $\sqrt{\sum_i |\hat{R}_i|^2}$ [Fig. 9(b)]. Intriguingly, orientation variance σ_{oo} [Fig. 15(b)] faintly indicates [analogously to Fig. 13(b)] the white matter tract interiors, by the orientation change inside high curvature paths (such as the genu of the corpus callosum (“GCC”). Tract interfaces previously highlighted by the AO measure [Fig. 10(d)] are also clearly marked. For reasons not yet clear to us, the shape and orientation covariance σ_{so}

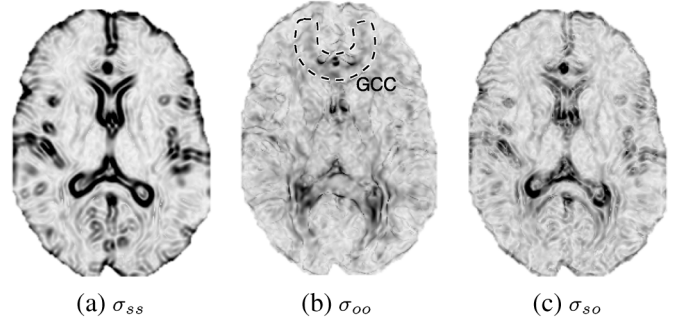


Fig. 15. Aggregate covariance measures evaluated on DTI slice: shape variance σ_{ss} (a), orientation variance σ_{oo} (b), and shape and orientation covariance σ_{so} (c). The orientation variance (b) faintly shows the presence of curved fiber tracts such as the genu of the corpus callosum (“GCC”), as well (more vividly) the tract interfaces previously detected with Adjacent Orthogonality (AO) measure (Fig. 10(d)). Numerical ranges for (a), (b), and (c) are $[0, 6.0]$, $[0, 1.8]$, and $[0, 1.9] \times 10^{-9} \text{ mm}^4/\text{s}^2$, respectively.

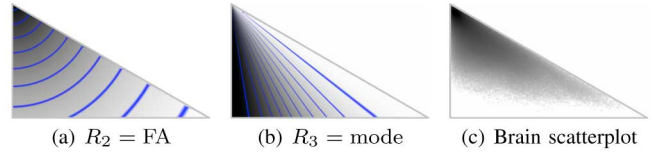


Fig. 16. Synthetic data for noise covariance analysis. $R_1 = |\mathbf{D}|$ is fixed, FA (a) and mode (b) vary through $[0, 1]$ and $[-1, 1]$, respectively. (c) Is a scatterplot of the brain dataset (in previous figures) in the same tensor shape domain. (a) $R_2 = \text{FA}$; (b) $R_3 = \text{mode}$; (c) brain scatterplot.

[Fig. 15(c)] also indicates major features like the white and gray matter interface.

We also apply our covariance tensor analysis to distributions of tensors estimated from noisy DWIs, and determine general patterns of covariance via a synthetic dataset sampling all possible tensor shapes, shown in Fig. 16. Similar to Fig. 1, this dataset has $R_1 = |\mathbf{D}|$ fixed at $0.0015 \text{ mm}^2/\text{s}$ (consistent with eigenvalues in the brain parenchyma [2]), with a constant baseline T2 value, and $R_2 = \text{FA}$ and $R_3 = \text{mode}$ vary over their full ranges. Fig. 16(c) maps the brain dataset used in previous figures to a scatterplot spanning the same tensor shape domain, to illustrate the broad diversity of tensor shapes that constitute typical datasets. DWIs were simulated using a single baseline and six icosahedral gradient directions \mathbf{g}_i [78] at $b = 1000 \text{ s}/\text{mm}^2$. Complex-valued Gaussian noise ($\text{SNR} = 50$ in the baseline image) was added to the real values synthesized from the standard single-tensor model $S_i = S_0 \exp(-b\mathbf{g}_i^T \mathbf{D} \mathbf{g}_i)$ [1]. Measurements were simulated 30 000 times and tensors were estimated by log-linear least squares fitting of the magnitude images [1], generating for each pixel a fourth-order covariance tensor Σ , and variances of R_2 and R_3 . The gradients $\{\mathbf{g}_i\}$ were randomly rotated (as a rigid set) for each measurement, to remove directional bias [79].

Fig. 17 depicts the results from our experiment. Only the (shape-related) upper-left corner of the covariance matrix is shown; orientation-related portions will be presented in future work. With our experimental design, the variance along R_1 (Σ_{11}) is generally larger than the variance along R_2 (Σ_{22}) or R_3 (Σ_{33}). Note also that Σ_{22} and Σ_{33} have comparable values. That is, for all possible tensor shapes (recall Fig. 1),

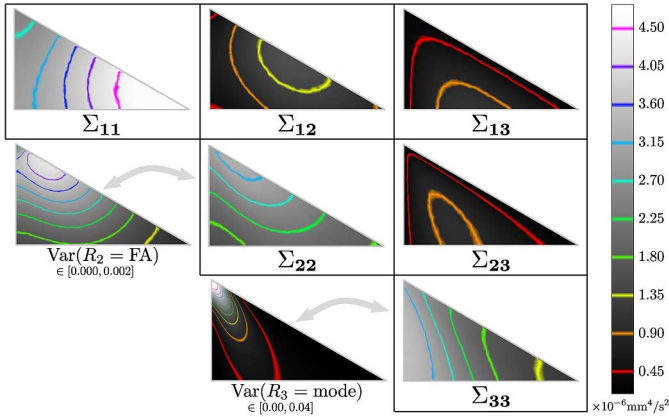


Fig. 17. Experimental results for shape-related covariance tensor components Σ_{ij} . Notably, the variance along tensor mode (R_3) is generally no larger than the variance along FA (R_2). Color scale for Σ_{ij} shown on right. $\text{Var}(R_2)$ is similar to Σ_{22} , but the $\text{Var}(R_3)$ diverges from Σ_{33} because of large $|\nabla R_3(\mathbf{D})|$ near isotropy. $\text{Var}(R_2)$ and $\text{Var}(R_3)$ use separate (and dimensionless) color scales than those used for the Σ_{ij} .

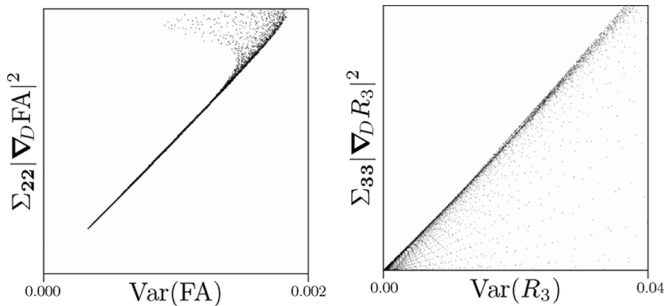


Fig. 18. Experimental accuracy of invariant variance approximation (39). The approximation is worst near isotropic tensors, where the directions of ∇R_2 and ∇R_3 vary most rapidly.

the variance *along* $\widehat{\nabla}_D R_3$ is similar to that along $\widehat{\nabla}_D R_2$. The parameterization of R_3 , however, makes its variance much larger than that of $R_2 = \text{FA}$ [recall (39)], consistent with earlier descriptions of noise sensitivity in eigenvalue skewness [60]. Scatterplots of $\text{Var}(J)$ and $\nabla_D J : \Sigma : \nabla_D J$ for invariants R_2 and R_3 (Fig. 18) illustrate the accuracy of our direct approximation to the variance of an invariant. The accuracy of the approximation is entirely determined by the accuracy of the first-order Taylor expansion. For example, the approximation fails for FA near isotropic tensors where the FA isocontours have high curvature [Fig. 16(a)].

V. DISCUSSION

Our framework of invariant gradients and rotation tangents gives mathematical representation (as an orthonormal coordinate system) to intuitive notions of tensor *shape* and *orientation*, effectively converting questions about shape and orientation into tensor contractions with particular basis tensors in Sym_3 . For example, the aggregate measure of shape and orientation covariance σ_{so} [(44), Fig. 15(c)] converts the question “How much are tensor shape and orientation changing simultaneously?” to tensor contractions along particular pairs of axes, creating a direct way to assess a meaningful property of the otherwise unwieldy fourth-order covariance tensor Σ . With a

multitude of tensor contractions and measures possible, Section V-A gives some guidance on various applications. Finally, Section V-B considers the significance of positive-definiteness in DTI processing, and the relationship between our work and recent Riemannian approaches.

A. Future Directions for Application

The quantitative summary in Fig. 11 of the normalized average gradient strengths throughout the brain is a starting point for considering applications of our framework. Knowing from Fig. 5(b) and Fig. 9(b) that R_1 indicates primarily the CSF boundary (not internal white matter structure), yet knowing from Fig. 11 that $\nabla \widehat{R}_1$ creates on average about 40% of the total gradient magnitude $|\nabla \mathbf{F}|$, one may consider omitting R_1 from DTI processing for studying white matter architecture. A similar argument could be made regarding K_1 and ∇K_1 . Some work already employs this strategy of leaving overall tensor size out of algorithmic processing, such as the normalized tensor scalar product (NTSP) difference measure of Jonasson *et al.* [25], or the use of the tensor deviatoric by Zhang *et al.* in tensor registration [35].

More generally, our work provides the means of modulating the role of tensor size, or any other tensor attribute, in the context of tensor differences [Section II-C], gradients [Section III-A], and covariance [Section III-B], as informed by anatomical specificity (Fig. 9), overall strength (Fig. 11), or noise sensitivity (Fig. 17). For example, in many approaches to nonlinear edge-preserving filtering, some measure of gradient strength controls the amount of local diffusive smoothing [80]. Fig. 9 suggests a possible way to scale the relative contributions of the six components of $\nabla \mathbf{F}$, as decomposed by our framework: $\nabla \widehat{R}_1$ can be scaled down to be comparable to $\nabla \widehat{R}_2$ in magnitude, $\nabla \widehat{\phi}_1$ and $\nabla \widehat{\phi}_2$ could be projected out entirely, and $\nabla \widehat{\phi}_3$ and $\nabla \widehat{R}_3$ could be combined into AO (Fig. 10). Along these same lines, Schultz *et al.* leverage our framework (as described in [40]) to tune the gradient components for computing structure tensors in DTI, improving the anatomical relevance of both level-set segmentation and edge-preserving filtering [67]. Alternatively, in the context of tuning a tensor difference measure for registering different datasets in a group study, it may be better to increase the relative significance of tensor orientation (as parameterized by the rotation tangents), so that tensor shape differences do not influence registration in a way that could confound the subsequent comparison of tissue organization (usually parameterized by anisotropy measures such as FA).

There are other possible applications of our gradient tensor analysis. Analytically measuring spatial derivatives of tensor invariants permits computer vision methods to extract the anisotropic structure of the tensor field in the *continuous* domain. Wherever edge detection or other feature extraction algorithms call for the image gradient, (27) and Section III-C provide the means of accurately calculating, for example, $\nabla |\mathbf{D}|$ or ∇FA . Early work along these lines shows that crease features (ridge and valley surfaces) of FA delimit the major white matter structures [81]. Also, with some refinements, the AO measure may help extract anatomical landmarks around the tract boundaries highlighted in Fig. 10(d). This could

guide nonrigid registration, given the importance of correctly registering neighboring yet distinct fiber tracts.

The ability to modulate the relative significance of different tensor attributes can also help in applications of the fourth-order covariance tensor. For example, Lenglet *et al.* [26] use the covariance tensor Σ (on a Riemannian manifold) to characterize regions in level-set DTI segmentation. It may be beneficial to decrease the significance of orientation variance relative to shape variance [measured by $\Sigma_{i,j=1,2,3}$ (37)], since tensors with similar shape but slightly differing orientations can belong to the same tract. Here too, AO can help detect distinctly oriented neighboring tracts so that they are not segmented together. Our image neighborhood covariance measurements (Figs. 12 and 14) may also have utility in brain tumor characterization and segmentation, where pathology can be characterized by simultaneous reductions in anisotropy (due to nervous tissue damage) and increases in diffusivity (due to edema) [51]; this covariance is captured exactly by Σ_{12} .

We plan to use our covariance decomposition to explore the effect of noise on tensor estimation, and to study DWI experimental design, as preliminarily demonstrated in Fig. 17. Previous work studies variances of specific tensor attributes [68], [69], [71], or the full fourth-order covariance tensor [37], [38]. Our framework blends these approaches by looking at components of the covariance tensor along the axes (in Sym_3) spanned by variations in tensor attributes, while avoiding the influence of the parameterization of those attributes. We can thus more fundamentally compare relative noise sensitivities along $\widehat{\nabla}_D R_2$ (measured by Σ_{22}) and tensor mode $\widehat{\nabla}_D R_3$ (Σ_{33}), independent of the parameterizations of R_2 and R_3 . Fig. 17 shows that for the chosen experimental design, Σ_{22} and Σ_{33} are not drastically different, even though the variance of mode can be an order of magnitude greater than the variance of FA. This suggests that, properly analyzed, tensor mode (R_3) could play as significant a role as FA (R_2) in quantitative DTI studies. Space does not permit similar exploration of orientation variance due to noise [measured separately by $\Sigma_{i,j=4,5,6}$ (37) or collectively by σ_{oo} (43)], but we are currently developing measures of orientation variance comparable to those developed for individual eigenvectors [68], [72].

B. Relationship to Riemannian Approaches

Our framework is “Euclidean” in that we consider diffusion tensors as elements of vector space Sym_3 , even though this overlooks the positive-definiteness of diffusion. This simplifying assumption has established precedent in the DTI literature [37], [38], [62], even in the context of reconstructing tensors from discrete samples [34], [73]. In an alternative approach to DTI analysis, tensors are located either implicitly or explicitly on a Riemannian manifold endowed with some metric that effectively creates an infinite distance between valid tensors and those with zero determinant [26], [63], [64], [66], [82], [83]. The relative merit of these approaches (Euclidean versus Riemannian) is not addressed here, as doing so would require a lengthier treatment of both Riemannian geometry theory and image processing practice than space allows. However, some basic points bear consideration.

On one hand, tensor invariants can be defined on Riemannian manifolds, and their gradients can be measured with respect to the local metric tensor, as can the angles between gradients [84]. In this sense, it is theoretically possible to redefine our framework entirely in a Riemannian context, which is a current topic of interest for us. On the other hand, the difference between Euclidean and Riemannian approaches may be viewed simply as a difference in choosing whether to enforce positive-definiteness solely during data acquisition, or also during analysis. Positive-definiteness is a fundamental property of Riemannian tensor analysis, enforced by a particular choice of the manifold metric. Euclidean approaches assume that positive-definiteness has already been enforced after acquisition, and may use measures that are defined without regard to positive-definiteness. Our tensor data is positive-definite mainly due to high signal-to-noise imaging, but also by clamping the rare negative eigenvalue to a machine-precision positive number during tensor estimation. More sophisticated approaches to positive-definite tensor estimation have been studied [85]–[88]. We also note that metrics like trace and FA are defined without respect to positive-definiteness [both are positive for $(\lambda_1, \lambda_2, \lambda_3) = (1.0, 1.0, -0.1)$], which has apparently not hindered their clinical utility. Finally, apart from the spline-based tensor interpolation [34] (which does not enforce positive-definiteness), our method focuses entirely on describing differences, gradients, and sample covariance of given tensors, rather than generating new tensors, which may mitigate the urgency of enforcing positive-definiteness.

APPENDIX A

ORTHOGONALITY OF $\Phi_i(\mathbf{D})$ AND INVARIANT GRADIENTS

The rotation tangents $\Phi_i(\mathbf{D})$ (Section II-B) are mutually orthogonal: $\Phi_i : \Phi_j = 0$ if $i \neq j$. For example

$$\begin{aligned} \Phi_1 : \Phi_2 &= (\lambda_2 - \lambda_3)(\mathbf{e}_2 \otimes \mathbf{e}_3 + \mathbf{e}_3 \otimes \mathbf{e}_2) \\ &\quad : (\lambda_3 - \lambda_1)(\mathbf{e}_3 \otimes \mathbf{e}_1 + \mathbf{e}_1 \otimes \mathbf{e}_3) \\ &= (\lambda_2 - \lambda_3)(\lambda_3 - \lambda_1) \\ &\quad \times (\mathbf{e}_2 \otimes \mathbf{e}_3 : \mathbf{e}_3 \otimes \mathbf{e}_1 + \mathbf{e}_3 \otimes \mathbf{e}_2 : \mathbf{e}_3 \otimes \mathbf{e}_1 + \mathbf{e}_2 \otimes \mathbf{e}_3 \\ &\quad \quad : \mathbf{e}_1 \otimes \mathbf{e}_3 + \mathbf{e}_3 \otimes \mathbf{e}_2 : \mathbf{e}_1 \otimes \mathbf{e}_3) \\ &= (\lambda_2 - \lambda_3)(\lambda_3 - \lambda_1) \\ &\quad \times (\delta_{23}\delta_{31} + \delta_{33}\delta_{21} + \delta_{21}\delta_{33} + \delta_{31}\delta_{23}) \\ &= 0. \end{aligned}$$

This uses the easily verified identity

$$\mathbf{e}_i \otimes \mathbf{e}_j : \mathbf{e}_k \otimes \mathbf{e}_l = \delta_{ik}\delta_{jl}. \quad (47)$$

To show that invariant gradients are orthogonal to rotation tangents, we first derive an expression for the gradient of an eigenvalue. A related analysis appears in Appendix A of [72]. The eigenvalues are unsorted in the following. From the spectral decomposition and (47), for a fixed n

$$\mathbf{D} : \mathbf{e}_n \otimes \mathbf{e}_n = \lambda_i \mathbf{e}_i \otimes \mathbf{e}_i : \mathbf{e}_n \otimes \mathbf{e}_n = \lambda_n \quad (48)$$

thus

$$\frac{\partial \lambda_n}{\partial \mathbf{D}} = \frac{\partial}{\partial \mathbf{D}} (\mathbf{D} : \mathbf{e}_n \otimes \mathbf{e}_n). \quad (49)$$

Then, assuming a *fixed* eigenvector \mathbf{e}_n , with the product rule

$$\begin{aligned} \frac{\partial \lambda_n}{\partial \mathbf{D}} &= \frac{\partial \mathbf{D}}{\partial \mathbf{D}} : \mathbf{e}_n \otimes \mathbf{e}_n + \mathbf{D} : \frac{\partial}{\partial \mathbf{D}} (\mathbf{e}_n \otimes \mathbf{e}_n) \\ &= \mathbf{I} : \mathbf{e}_n \otimes \mathbf{e}_n + \mathbf{D} : \mathbf{0} \\ &= \mathbf{e}_n \otimes \mathbf{e}_n. \end{aligned} \quad (50)$$

We can then express the gradient of any invariant J by applying the chain rule to the spectral decomposition

$$\nabla_D J = \frac{\partial J}{\partial \mathbf{D}} = \frac{\partial J}{\partial \lambda_i} \frac{\partial \lambda_i}{\partial \mathbf{D}} = \frac{\partial J}{\partial \lambda_i} (\mathbf{e}_i \otimes \mathbf{e}_i). \quad (51)$$

Then (17)–(19), (47), and (51) imply

$$\nabla_D J : \hat{\Phi}_i = 0. \quad (52)$$

APPENDIX B

SHAPE AND ORIENTATION NEAR ROTATIONAL SYMMETRY

The framework of invariant gradients and rotation tangents is well defined when the tensor eigenvalues are unequal, as is always the case in numerical measured data. Certain distinctions between shape and orientation, however, gradually become ambiguous as rotational symmetry develops. A two-dimensional example illustrates this.

Two-dimensional symmetric tensors have three degrees-of-freedom. The definitions of K_1 and K_2 in (10) also apply to two-dimensional tensors, giving two orthogonal invariants that parameterize tensor shape in terms of size and 2-D anisotropy. In two dimensions, K_2 reduces to

$$K_2(\mathbf{D}) = (\lambda_1 - \lambda_2)/\sqrt{2} \quad (53)$$

and then (50) implies

$$\widehat{\nabla}_D K_2(\mathbf{D}) = (\mathbf{e}_1 \otimes \mathbf{e}_1 - \mathbf{e}_2 \otimes \mathbf{e}_2)/\sqrt{2} \quad (54)$$

where $\{\lambda_i\}, \{\mathbf{e}_i\}$ is the eigensystem of \mathbf{D} , and $\lambda_1 \geq \lambda_2$. The rotation tangent for the single axis of rotation is, as in (22)

$$\hat{\Phi}(\mathbf{D}) = (\mathbf{e}_1 \otimes \mathbf{e}_2 + \mathbf{e}_2 \otimes \mathbf{e}_1)/\sqrt{2}. \quad (55)$$

Let \mathbf{D}_0 be a two-dimensional tensor with eigenvalues $\{\lambda + \varepsilon, \lambda - \varepsilon\}$ and eigenvectors $\{\mathbf{b}_1, \mathbf{b}_2\}$, which form basis \mathcal{B}

$$[\mathbf{D}_0]_{\mathcal{B}} = \begin{bmatrix} \lambda + \varepsilon & 0 \\ 0 & \lambda - \varepsilon \end{bmatrix}. \quad (56)$$

Let \mathbf{D}_1 be the rotation of \mathbf{D}_0 by $\pi/4$

$$[\mathbf{D}_1]_{\mathcal{B}} = \begin{bmatrix} \frac{1}{\sqrt{2}} & -\frac{1}{\sqrt{2}} \\ \frac{1}{\sqrt{2}} & \frac{1}{\sqrt{2}} \end{bmatrix} [\mathbf{D}_0]_{\mathcal{B}} \begin{bmatrix} \frac{1}{\sqrt{2}} & \frac{1}{\sqrt{2}} \\ -\frac{1}{\sqrt{2}} & \frac{1}{\sqrt{2}} \end{bmatrix} = \begin{bmatrix} \lambda & \varepsilon \\ \varepsilon & \lambda \end{bmatrix}. \quad (57)$$

As the diagonalization of $[\mathbf{D}_1]_{\mathcal{B}}$, (57) implies that the eigenvectors of \mathbf{D}_1 are $\mathbf{e}_1 = (\mathbf{b}_1 + \mathbf{b}_2)/\sqrt{2}$ and $\mathbf{e}_2 = (-\mathbf{b}_1 + \mathbf{b}_2)/\sqrt{2}$. Then, from (55)

$$\begin{aligned} \hat{\Phi}(\mathbf{D}_1) &= (\mathbf{e}_1 \otimes \mathbf{e}_2 + \mathbf{e}_2 \otimes \mathbf{e}_1)/\sqrt{2} \\ &= ((-\mathbf{b}_1 + \mathbf{b}_2) \otimes (\mathbf{b}_1 + \mathbf{b}_2) \\ &\quad + (\mathbf{b}_1 + \mathbf{b}_2) \otimes (-\mathbf{b}_1 + \mathbf{b}_2))/(2\sqrt{2}) \\ &= (-\mathbf{b}_1 \otimes \mathbf{b}_1 + \mathbf{b}_2 \otimes \mathbf{b}_2)/\sqrt{2} \\ &= -\widehat{\nabla}_D K_2(\mathbf{D}_0). \end{aligned} \quad (58)$$

That is, the K_2 invariant gradient at \mathbf{D}_0 is parallel to the rotation tangent at \mathbf{D}_1 . However, by (56) and (57), the distance between \mathbf{D}_0 and \mathbf{D}_1 is arbitrarily small

$$|\mathbf{D}_1 - \mathbf{D}_0| = 2\varepsilon \quad (59)$$

In summary, the number of degrees-of-freedom in the tensor never changes, but near rotational symmetry ($\lambda_1 \approx \lambda_2$), the otherwise clear distinction between variation in shape (along $\widehat{\nabla}_D K_2$) and orientation (along $\hat{\Phi}$) becomes ambiguous.

Analogous situations arise in three dimensions when tensor mode [(11) and Fig. 1] approaches its extrema. Invariant gradient $\widehat{\nabla}_D K_3$ and rotation tangent $\hat{\Phi}_3$ become interchangeable as tensor mode K_3 approaches -1 ($\lambda_1 \approx \lambda_2$; rotational symmetry of planar anisotropy around \mathbf{e}_3). $\widehat{\nabla}_D K_3$ and $\hat{\Phi}_3$ still span two degrees-of-freedom, but the orientation of $\widehat{\nabla}_D K_3$ and $\hat{\Phi}_3$ within their span is essentially arbitrary. This ambiguity is actually leveraged in Section III-A for defining the AO measure. Similarly, $\widehat{\nabla}_D K_3$ and $\hat{\Phi}_1$ become interchangeable as tensor mode K_3 approaches $+1$ ($\lambda_2 \approx \lambda_3$; rotational symmetry of linear anisotropy around \mathbf{e}_1). In addition, when K_2 or R_2 approaches zero ($\lambda_1 \approx \lambda_2 \approx \lambda_3$), $\widehat{\nabla}_D K_1$ and $\widehat{\nabla}_D R_1$ remain stable, though all other invariant gradients and rotation tangents become interchangeable. $\widehat{\nabla}_D K_1 = \mathbf{I}$ is constant, but $\widehat{\nabla}_D R_1$ becomes unstable when R_1 approaches zero (which never happens in diffusive tissue).

ACKNOWLEDGMENT

The authors would like to thank the anonymous reviewers for their feedback, and discussion with R. San José Estépar, L. O'Donnell, Dr. A. Golby, and Dr. I.-F. Talos. DWI data courtesy of Dr. S. Mori, Johns Hopkins University, Baltimore, MD.

REFERENCES

- [1] P. J. Basser, J. Mattiello, and D. LeBihan, "Estimation of the effective self-diffusion tensor from the NMR spin-echo," *J. Magn. Reson., Series B*, vol. 103, no. 3, pp. 247–254, 1994.

- [2] C. Pierpaoli, P. Jezzard, P. J. Basser, A. Barnett, and G. DiChiro, "Diffusion tensor MR imaging of the human brain," *Radiology*, vol. 201, no. 3, pp. 637–648, Dec 1996.
- [3] T. Klingberg, M. Hedehus, E. Temple, T. Salz, J. D. E. Gabrielli, M. E. Moseley, and R. A. Poldrack, "Microstructure of temporo-parietal white matter as a basis for reading ability: Evidence from diffusion tensor magnetic resonance imaging," *Neuron*, vol. 25, pp. 493–500, 2000.
- [4] R. A. A. Kanaan, J.-S. Kim, W. E. Kaufmann, G. D. Pearlson, G. J. Barker, and P. K. McGuire, "Diffusion tensor imaging in schizophrenia," *Biol. Psychiatry*, vol. 58, pp. 921–929, Dec. 2005.
- [5] D. H. Salat, D. S. Tuch, N. D. Hevelone, B. Fischl, S. Corkin, H. D. Rosas, and A. M. Dale, "Age-related changes in prefrontal white matter measured by diffusion tensor imaging," *Ann. NY Acad. Sci.*, vol. 1064, pp. 37–49, 2005.
- [6] A. S. Field, Y.-C. Wu, and A. L. Alexander, "Principal diffusion direction in peritumoral fiber tracts," *Ann. NY Acad. Sci.*, vol. 1064, pp. 193–201, 2005.
- [7] R. F. Dougherty, M. Ben-Shachar, G. Deutsch, P. Potanina, R. Bammer, and B. A. Wandell, "Occipital-callosal pathways in children: Validation and atlas development," *Ann. NY Acad. Sci.*, vol. 1064, pp. 98–112, 2005.
- [8] D. S. Tuch, D. H. Salat, J. J. Wisco, A. K. Zaleta, N. D. Hevelone, and H. D. Rosas, "Choice reaction time performance correlates with diffusion anisotropy in white matter pathways supporting visuospatial attention," *Proc. Nat. Acad. Sci.*, vol. 102, no. 34, pp. 12212–12217, 2005.
- [9] J. C. Walker, J. M. Guccione, Y. Jiang, P. Zhang, A. W. Wallace, E. W. Hsu, and M. B. Ratcliffe, "Helical myofiber orientation after myocardial infarction and left ventricular surgical restoration in sheep," *J. Thoracic Cardiovascular Surg.*, vol. 129, no. 2, pp. 382–390, 2005.
- [10] P. A. Helm, L. Younes, M. F. Beg, D. B. Ennis, C. Leclercq, O. P. Faris, E. McVeigh, D. Kass, M. I. Miller, and R. L. Winslow, "Evidence of structural remodeling in the dyssynchronous failing heart," *Circulation Res.*, vol. 98, no. 1, pp. 125–132, 2006.
- [11] M. E. Moseley, Y. Cohen, J. Mintorovitch, L. Chileuitt, H. Shimizu, J. Kucharczyk, M. F. Wendland, and P. R. Weinstein, "Early detection of regional cerebral ischemia in cats: Comparison of diffusion- and T2-weighted MRI and spectroscopy," *Magn. Reson. Med.*, vol. 14, no. 2, pp. 330–346, May 1990.
- [12] C. H. Sotak, "The role of diffusion tensor imaging in the evaluation of ischemic brain injury—A review," *Nucl. Magn. Reson. Biomed.*, vol. 15, pp. 561–569, 2002.
- [13] P. J. Basser, "Inferring microstructural features and the physiological state of tissues from diffusion-weighted images," *Nucl. Magn. Reson. Biomed.*, vol. 8, pp. 333–344, 1995.
- [14] C. Beaulieu, "The basis of anisotropic water diffusion in the nervous system—A technical review," *Nucl. Magn. Reson. Biomed.*, vol. 15, pp. 435–455, 2002.
- [15] C.-P. Lin, W.-Y. I. Tseng, H.-C. Cheng, and J.-H. Chen, "Validation of diffusion tensor magnetic resonance axonal fiber imaging with registered manganese-enhanced optic tracts," *NeuroImage*, vol. 14, pp. 1035–1047, 2001.
- [16] J. Dauguet, S. Peled, V. Berezovskii, T. Delzescaux, S. K. Warfield, R. Born, and C.-F. Westin, "3D histological reconstruction of fiber tracts and direct comparison with diffusion tensor MRI tractography," in *Proc. MICCAI 2006*, Copenhagen, Denmark, Oct. 2006, pp. 109–116.
- [17] E. W. Hsu, A. L. Muzikant, S. A. Matulevicius, R. C. Penland, and C. S. Henriquez, "Magnetic resonance myocardial fiber-orientation mapping with direct histological correlation," *Amer. J. Physiol.*, vol. 274, pp. 1627–1634, 1998.
- [18] D. F. Scollan, A. Holmes, R. Winslow, and J. Forder, "Histological validation of myocardial microstructure obtained from diffusion tensor magnetic resonance imaging," *Amer. J. Physiol.*, vol. 275, pp. 2308–2318, 1998.
- [19] D. Alexander, J. Gee, and R. Bajcsy, "Similarity measures for matching diffusion tensor images," in *Proc. Brit. Mach. Vis. Conf. (BMVC)*, Nottingham, U.K., Sep. 1999, pp. 93–102.
- [20] H. Zhang, P. A. Yushkevich, and J. C. Gee, "Registration of diffusion tensor images," in *Proc. CVPR 2004*, Jun. 2004, vol. 1, pp. 842–847.
- [21] C. Chéd'hotel, D. Tschumperlé, R. Deriche, and O. Faugeras, "Constrained flows of matrix-valued functions: Application to diffusion tensor regularization," in *Proc. 7th Eur. Conf. Comput. Vis.-Part I (ECCV '02)*, London, U.K., 2002, pp. 251–265.
- [22] Z. Wang and B. C. Vemuri, "An affine invariant tensor dissimilarity measure and its applications to tensor-valued image segmentation," in *Proc. CVPR 2004*, 2004, vol. 1, pp. 228–233.
- [23] M. Welk, J. Weickert, F. Becker, C. Schnörr, C. Feddern, and B. Burgeth, "Median and related local filters for tensor-valued images," *Signal Process.*, vol. 87, pp. 291–308, 2007.
- [24] M. R. Wiegell, D. S. Tuch, H. B. W. Larsson, and V. J. Wedeen, "Automatic segmentation of thalamic nuclei from diffusion tensor magnetic resonance imaging," *NeuroImage*, vol. 19, pp. 391–401, Jun. 2003.
- [25] L. Jonasson, X. Bresson, P. Hagmann, O. Cuisenaire, R. Meuli, and J.-P. Thiran, "White matter fiber tract segmentation in DT-MRI using geometric flows," *Med. Image Anal.*, vol. 9, pp. 223–236, 2005.
- [26] C. Lenglet, M. Rousson, and R. Deriche, "DTI segmentation by statistical surface evolution," *IEEE Trans. Med. Imag.*, vol. 25, no. 6, pp. 685–700, Jun. 2006.
- [27] H. Knutsson, "A tensor representation of 3-D structures," in *5th IEEE-ASSP EURASIP Workshop Multidimensional Signal Process.*, Noordwijkerhout, The Netherlands, Sep. 1987.
- [28] W. Förstner and E. Gülch, "A fast operator for detection and precise location of distinct points, corners and centres of circular features," in *Proc. ISPRS Intercommission Conf. Fast Process. Photogrammetric Data*, Interlaken, Switzerland, Jun. 1987, pp. 281–305.
- [29] J. Bigün and G. H. Granlund, "Optimal orientation detection of linear symmetry," in *Proc. IEEE 1st Int. Conf. Comput. Vision*, London, U.K., Jun. 1987, pp. 433–438.
- [30] L. O'Donnell, W. E. L. Grimson, and C.-F. Westin, "Interface detection in diffusion tensor MRI," in *Proc. MICCAI 2004*, 2004, pp. 360–367.
- [31] C. A. Castañero-Moraga, M. A. Rodrigues-Florida, L. Alvarez, C.-F. Westin, and J. Ruiz-Alzola, "Anisotropic interpolation of DT-MRI," in *Proceedings MICCAI 2004*, Rennes-Saint Malo, France, Sep. 2004.
- [32] C. Feddern, J. Weickert, B. Burgeth, and M. Welk, "Curvature-driven PDE methods for matrix-valued images," *Int. J. Comput. Vis.*, vol. 69, no. 1, pp. 93–107, Aug. 2006.
- [33] G. A. Holzapfel, *Nonlinear Solid Mechanics*. New York: Wiley, 2000.
- [34] S. Pajevic, A. Aldroubi, and P. J. Basser, "A continuous tensor field approximation of discrete DT-MRI data for extracting microstructural and architectural features of tissue," *J. Magn. Reson.*, vol. 154, pp. 85–100, 2002.
- [35] H. Zhang, P. A. Yushkevich, D. C. Alexander, and J. C. Gee, "Deformable registration of diffusion tensor MR images with explicit orientation optimization," *Med. Image Anal.*, vol. 10, no. 5, pp. 764–785, Oct. 2006.
- [36] C. Lenglet, M. Rousson, R. Deriche, O. D. Faugeras, S. Lehericy, and K. Ugurbil, "A riemannian approach to diffusion tensor images segmentation," in *Proc. IPMI 2005*, Glenwood Springs, CO, Jul. 2005, pp. 591–602.
- [37] P. J. Basser and S. Pajevic, "A normal distribution for tensor-valued random variables: Applications to diffusion tensor MRI," *IEEE Trans. Med. Imag.*, vol. 22, no. 7, pp. 785–794, Jul. 2003.
- [38] P. J. Basser and S. Pajevic, "Spectral decomposition of a 4th-order covariance tensor: Applications to diffusion tensor MRI," *Signal Process.*, vol. 87, pp. 220–236, 2007.
- [39] C. Lenglet, M. Rousson, R. Deriche, and O. Faugeras, "Statistics on the manifold of multivariate normal distributions: Theory and application to diffusion tensor MRI processing," *J. Math. Imag. Vis.*, vol. 25, no. 3, pp. 423–444, 2006.
- [40] G. L. Kindlmann, "Visualization and analysis of diffusion tensor fields" Ph.D. dissertation, Univ. Utah, Sep. 2004 [Online]. Available: <http://www.cs.utah.edu/research/techreports/2004/abstracts/UUCS-04-014a.pdf>
- [41] D. B. Ennis and G. Kindlmann, "Orthogonal tensor invariants and the analysis of diffusion tensor magnetic resonance images," *Magn. Reson. Med.*, vol. 55, no. 1, pp. 136–146, 2006.
- [42] D. E. Bourne and P. C. Kendall, *Vector Analysis and Cartesian Tensors*, 3rd ed. Boca Raton, FL: CRC, 1992.
- [43] K. Hoffman and R. Kunze, *Linear Algebra*. Englewood Cliffs, NJ: Prentice-Hall, 1971.
- [44] J. Crank, *The Mathematics of Diffusion*. Oxford, U.K.: Oxford Univ., 1975.
- [45] D. S. Dummit and R. M. Foote, *Abstract Algebra*. Englewood Cliffs, NJ: Prentice-Hall, 1991.
- [46] A. J. M. Spencer, *Continuum Mechanics*, 5th ed. New York: Wiley, 1992.
- [47] J. C. Criscione, J. D. Humphrey, A. S. Douglas, and W. C. Hunter, "An invariant basis for natural strain which yields orthogonal stress response terms in isotropic hyperelasticity," *J. Mech. Phys. Solids*, vol. 48, pp. 2445–2465, 2000.
- [48] M. M. Bahn, "Invariant and orthonormal scalar measures derived from magnetic resonance diffusion tensor imaging," *J. Magn. Reson.*, vol. 141, pp. 68–77, 1999.

- [49] G. Thomalla, V. Glauche, M. A. Koch, C. Beaulieu, C. Weiller, and J. Röther, "Diffusion tensor imaging detects early Wallerian degeneration of the pyramidal tract after ischemic stroke," *NeuroImage*, vol. 22, no. 4, pp. 1767–1774, Aug. 2004.
- [50] M. Kubicki, C.-F. Westin, S. E. Maier, H. Mamata, M. Frumin, H. Ernst-Hirschfeld, R. Kikinis, F. A. Jolesz, R. W. McCarley, and M. E. Shenton, "Cingulate fasciculus integrity disruption in schizophrenia: A magnetic resonance diffusion tensor imaging study," *Biol. Psychiatry*, vol. 54, pp. 1171–1180, 2003.
- [51] S. Lu, D. Ahn, G. Johnson, M. Law, D. Zagzag, and R. I. Grossman, "Diffusion-tensor MR imaging of intracranial neoplasia and associated peritumoral edema: Introduction of the tumor infiltration index," *Neuroradiology*, vol. 232, no. 1, pp. 221–228, Jul. 2004.
- [52] S. M. Smith, M. Jenkinson, H. Johansen-Berg, D. Rueckert, T. E. Nichols, C. E. Mackay, K. E. Watkins, O. Ciccarelli, M. Z. Cader, P. M. Matthews, and T. E. J. Behrens, "Tract-based spatial statistics: Voxelwise analysis of multi-subject diffusion data," *NeuroImage*, vol. 31, pp. 1487–1505, 2006.
- [53] G. Kindlmann, "Superquadric tensor glyphs," in *Proc. IEEE TVCG/EG Symp. Visualization 2004*, May 2004, pp. 147–154.
- [54] D. B. Ennis, G. Kindlmann, I. Rodriguez, P. A. Helm, and E. R. McVeigh, "Visualization of tensor fields using superquadric glyphs," *Magn. Reson. Med.*, vol. 53, pp. 169–176, Jan. 2005.
- [55] A. L. Alexander, K. M. Hasan, M. Lazar, J. S. Tsuruda, and D. L. Parker, "Analysis of partial volume effects in diffusion-tensor MRI," *Magn. Reson. Med.*, vol. 45, pp. 770–780, 2001.
- [56] D. C. Alexander, G. J. Barker, and S. R. Arridge, "Detection and modeling of non-gaussian apparent diffusion coefficients profiles in human brain data," *Magn. Reson. Med.*, vol. 48, pp. 331–340, 2002.
- [57] D. S. Tuch, R. M. Weisskoff, J. W. Belliveau, and V. J. Wedeen, "High angular resolution diffusion imaging of the human brain," in *Proc. ISMRM 1999*, 1999, p. 321.
- [58] M. R. Wiegell, H. B. W. Larsson, and V. J. Wedeen, "Fiber crossing in human brain depicted with diffusion tensor MR imaging," *Radiology*, vol. 217, no. 3, pp. 897–903, Dec. 2000.
- [59] D. S. Tuch, T. G. Reese, M. R. Wiegell, N. Makris, J. W. Belliveau, and V. J. Wedeen, "High angular resolution diffusion imaging reveals intravoxel white matter fiber heterogeneity," *Magn. Reson. Med.*, vol. 48, pp. 577–582, 2002.
- [60] P. J. Basser and D. K. Jones, "Diffusion-tensor MRI: Theory, experimental design and data analysis—A technical review," *Nucl. Magn. Reson. Biomed.*, vol. 15, pp. 456–467, 2002.
- [61] T. E. Conturo, N. F. Lori, T. S. Cull, E. Akbudak, A. Z. Snyder, J. S. Shimony, R. C. McKinstry, H. Burton, and M. E. Raichle, "Tracking neuronal fiber pathways in the living human brain," *Proc. Nat. Acad. Sci.*, vol. 96, pp. 10422–10427, Aug. 1999.
- [62] P. J. Basser, S. Pajevic, C. Pierpaoli, J. Duda, and A. Aldroubi, "In vivo fiber tractography using DT-MRI data," *Magn. Reson. Med.*, vol. 44, pp. 625–632, 2000.
- [63] P. T. Fletcher and S. Joshi, "Principal geodesic analysis on symmetric spaces: Statistics of diffusion tensors," in *Proceedings ECCV 2004 Workshop Comput. Vision Approaches to Medical Image Analysis (CVAMIA)*. New York: Springer-Verlag, 2004, vol. 31107, Lecture Notes Computer Science, pp. 87–98.
- [64] P. G. Batchelor, M. Moakher, D. Atkinson, F. Calamante, and A. Connelly, "A rigorous framework for diffusion tensor calculus," *Magn. Reson. Med.*, vol. 53, no. 1, pp. 221–225, Jan. 2005.
- [65] X. Pennec, P. Fillard, and N. Ayache, "A riemannian framework for tensor computing," *Int. J. Comput. Vis.*, vol. 66, no. 1, pp. 41–66, Jan. 2006.
- [66] V. Arsigny, P. Fillard, X. Pennec, and N. Ayache, "Log-Euclidean metrics for fast and simple calculus on diffusion tensors," *Magn. Reson. Med.*, vol. 56, no. 2, pp. 411–421, Aug. 2006.
- [67] T. Schultz, B. Burgeth, and J. Weickert, "Flexible segmentation and smoothing of DT-MRI fields through a customizable structure tensor," in *Advances in Visual Computing (Proceedings of the Second International Symposium on Visual Computing)*. New York: Springer, 2006, vol. 4291, Lecture Notes in Computer Science.
- [68] L.-C. Chang, C. G. Koay, C. Pierpaoli, and P. J. Basser, "Variance of estimated DTI-derived parameters via first-order perturbation methods," *Magn. Reson. Med.*, vol. 57, pp. 141–149, 2007.
- [69] C. Koay, L.-C. Chang, C. Pierpaoli, and P. J. Basser, "Error propagation framework for diffusion tensor imaging," in *Proc. ISMRM 2006*, 2006, p. 1067.
- [70] Y. Shen, I. Pu, and C. Clark, "Analytical expressions for noise propagation in diffusion tensor imaging," in *Proc. ISMRM 2006*, 2006, p. 1065.
- [71] A. H. Poonawalla and X. J. Zhou, "Analytical error propagation in diffusion anisotropy calculations," *J. Magn. Reson. Imag.*, vol. 19, pp. 489–498, 2004.
- [72] A. W. Anderson, "Theoretical analysis of the effects of noise on diffusion tensor imaging," *Magn. Reson. Med.*, vol. 46, pp. 1174–1188, 2001.
- [73] A. Aldroubi and P. Basser, "Reconstruction of vector and tensor fields from sampled discrete data," *Contemporary Math.*, vol. 247, pp. 1–15, 1999.
- [74] M. Unser, A. Aldroubi, and M. Eden, "B-Spline signal processing: Part I—Theory," *IEEE Trans. Signal Process.*, vol. 41, no. 2, pp. 821–833, Feb. 1993.
- [75] M. Unser, A. Aldroubi, and M. Eden, "B-Spline signal processing: Part II—efficient design and applications," *IEEE Trans. Signal Process.*, vol. 41, no. 2, pp. 834–848, Feb. 1993.
- [76] S. Pajevic and C. Pierpaoli, "Color schemes to represent the orientation of anisotropic tissues from diffusion tensor data: Application to white matter fiber tract mapping in the human brain," *Magn. Reson. Med.*, vol. 42, no. 3, pp. 526–540, 1999.
- [77] S. Mori, S. Wakana, L. Nagae-Poetscher, and P. V. Zijl, *MRI Atlas of Human White Matter*. New York: Elsevier, 2005.
- [78] D. K. Jones, M. A. Horsfield, and A. Simmons, "Optimal strategies for measuring diffusion in anisotropic systems by magnetic resonance imaging," *Magn. Reson. Med.*, vol. 42, pp. 515–525, 1999.
- [79] D. K. Jones, "The effect of gradient sampling schemes on measures derived from diffusion tensor MRI: A Monte Carlo study," *Magn. Reson. Med.*, vol. 51, pp. 807–815, 2004.
- [80] P. Perona and J. Malik, "Scale-space and edge detection using anisotropy diffusion," *IEEE Trans. Pattern Anal. Mach. Intell.*, vol. 12, no. 7, pp. 629–639, Jul. 1990.
- [81] G. Kindlmann, X. Tricoche, and C.-F. Westin, "Anisotropy creases delineate white matter structure in diffusion tensor MRI," in *Proceedings MICCAI 2006*. New York: Springer-Verlag, 2006, vol. 4190, Lecture Notes Computer Science, pp. 126–133.
- [82] X. Pennec, Probabilities and statistics on Riemannian manifolds: A geometric approach INRIA, Sophia Antipolis, France, Tech. Rep. 5093, Jan. 2004.
- [83] P. Fillard, V. Arsigny, X. Pennec, and N. Ayache, "Clinical DT-MRI estimation, smoothing and fiber tracking with log-euclidean metrics," in *Proc. ISBI 2006*, Arlington, VA, Apr. 2006, pp. 786–789.
- [84] M. P. do Carmo, *Riemannian Geometry*. Boston, MA: Birkhäuser, 1992.
- [85] D. Tschumperlé and R. Deriche, "DT-MRI images: Estimation, regularization and application," in *Proceedings EUROCAST*. New York: Springer-Verlag, 2003, vol. 2809, Lecture Notes Computer Science, pp. 530–541.
- [86] Z. Wang, B. C. Vemuri, Y. Chen, and T. H. Mareci, "A constrained variational principle for direct estimation and smoothing of the diffusion tensor field from complex DWI," *IEEE Trans. Med. Imag.*, vol. 23, no. 8, pp. 930–939, Aug. 2004.
- [87] C. G. Koay, J. D. Carew, A. L. Alexander, P. J. Basser, and M. E. Meyerand, "Investigation of anomalous estimates of tensor-derived quantities in diffusion tensor imaging," *Magn. Reson. Med.*, vol. 55, pp. 930–936, 2006.
- [88] M. Niethammer, R. San Jose Estepar, S. Bouix, M. Shenton, and C.-F. Westin, "On diffusion tensor estimation," in *Proc. 28th IEEE EMBS*, Aug. 2006, pp. 2622–2625.